The optical properties, physical properties and direct radiative forcing of urban columnar aerosols in the Yangtze River Delta, China

Bingliang Zhuang[1, *], Tijian Wang[1, **], Jane. Liu[1, 2], Huizheng Che[3], Yong Han[1], Yu Fu[4], Shu Li[1], Min Xie[1], Mengmeng Li[1], Pulong Chen[1], Huimin Chen[1], Xiu-qun Yang[1], Jianning Sun[1]

[1] School of Atmospheric Sciences, CMA-NJU Joint Laboratory for Climate Prediction Studies, Jiangsu Collaborative Innovation Center for Climate Change, Nanjing University, Nanjing 210023, China

[2] Department of Geography and Planning, University of Toronto, Toronto, M5S 3G3, Canada

[3] Key Laboratory of Atmospheric Chemistry (LAC), Chinese Academy of Meteorological Sciences (CAMS), CMA, Beijing, 100081, China

[4] Dalian Weather Modification Office, Dalian, 116001, China

[*] Corresponding author, E-mail: blzhuang@nju.edu.cn; Tel.: +862589681156; Fax: +862589683797

[* *]Corresponding author, E-mail: tjwang@nju.edu.cn; Tel.: +862589683797; Fax: +862589683797

Abstract: The optical and physical properties as well as the direct radiative forcings (DRF) of fractionated aerosols in the urban area of the western Yangtze River Delta (YRD) are investigated with measurements from a Cimel sun photometer combined with a radiation transfer model. Ground-based observations of aerosols have much higher temporal resolutions than satellite retrievals. An initial analysis reveals the characteristics of the optical properties of different types of fractionated aerosols in western YRD. The total aerosols, mostly composed by scattering components (93.8%), have a mean optical depth of 0.65 at 550nm and refractive index of 1.44+0.0084i at 440 nm. The fine aerosols are approximately 4 times more abundant and have very different compositions from coarse aerosols. The absorbing components account for only ~4.6% of fine aerosols and 15.5% of coarse aerosols and have

smaller sizes than the scattering aerosols within the same mode. Therefore, fine particles have stronger scattering than coarse ones, simultaneously reflecting the different size distributions between the absorbing and scattering aerosols. The relationships among the optical properties quantify the aerosol mixings and imply that approximately 15% and 27.5% of the total occurrences result in dust and black carbon dominating mixing aerosols, respectively, in the western YRD. Unlike the optical properties, the size distributions of aerosols in the western YRD are similar to those found at other sites over eastern China on a climatological scale, peaking at radii of 0.148 and 2.94 μm. However, further analysis reveals that the coarse-dominated particles can also lead to severe haze pollution over the YRD. Observation-based estimations indicate that both fine and coarse aerosols in the western YRD exert a negative DRF, and this is especially true for fine aerosols (-11.17 W/m^2 at the top of atmosphere, TOA). A higher absorption fraction leads directly to the negative DRF being further offset for coarse aerosols (-0.33 W/m^2) at the TOA. Similarly, the coarse mode DRF contributes to only 13.3% of the total scattering aerosols but >33.7% to the total absorbing aerosols. Sensitivity analysis states that aerosol DRFs are not highly sensitive to their profiles in clear-sky conditions. Most of the aerosol properties and DRFs have substantial seasonality in the western YRD. The results further reveal the contributions of each component of the different size particles to the total aerosol optical depths (AODs) and DRFs. Additionally, these results can be used to improve aerosol modelling performance and the modelling of aerosol effects in the eastern regions of China.

1 Introduction

Atmospheric aerosols have significant influences on air quality, human health, and regional/global climate changes. Scientists have suggested that scattering aerosols could greatly offset the warming

effects of greenhouse gases (Kiehl and Briegleb, 1993) while absorbing aerosols might further exacerbate global warming (Jacobson 2002). The global mean direct radiative forcing (DRF) of scattering aerosols, fossil fuel black carbon (BC) and all aerosols was estimated to be approximately -0.55, +0.2 and -1.04 W/m^2, respectively (Forster et al., 2007; Reddy et al., 2005), at the top of atmosphere (TOA), thus changing atmospheric circulations and the hydrological cycle in different ways (Menon et al., 2002; Wang et al., 2015).

Many studies of aerosol radiative forcing and its climate effects have been carried out over the past two decades at both global and regional scales based on model simulations and observations (e.g., Penner et al., 2001; Bellouin et al., 2003; Liao and Seinfeld, 2005; Wu et al., 2012; Wang et al., 2015; etc.); however, large uncertainties remain. Forster et al. (2007) noted that the global mean DRF varied from +0.04 to -0.63 W/m^2 for total aerosols and from +0.1 to +0.3 W/m^2 for BC. The ranges were larger at regional scales, especially in high aerosol emission regions (Zhuang et al., 2013a). The DRF uncertainties subsequently result in large biases of the aerosol-related climate effects. There are many factors that affect the simulated radiative forcing, including the aerosol optical properties, which are related to aerosol emissions, size distributions, profiles, compositions, and mixing states (Holler et al., 2003; Ma et al., 2017), as well as the surface albedo and clouds (Ma and Yu, 2012; Forster et al., 2007). The related uncertainties could be substantially reduced if the observed aerosol optical properties were determined and used (Forster et al., 2007).

With the rapid increase in population and economic growth, air pollutant emissions are much higher in East Asia than in other regions (Zhang et al., 2009). Additionally, dust aerosols from desert regions are always transported to northern and eastern China or even further afield (Wang et al., 2009; Sun et al., 2012; Li et al., 2015a). Consequently, aerosols in China frequently experience large loadings

and complicated compositions and spatial distributions (Zhang et al., 2012), especially in urban agglomerations or megacities (e.g., the Yangtze River Delta, YRD). Therefore, the aerosol optical properties in the YRD must be clarified via observations, which is a premise for accurately estimating the radiative effects of aerosols and for improving aerosol model performance over the eastern region of China. Recently, numerous observation-based studies have been conducted on both surface (e.g., Bergin et al., 2001; Xu et al., 2002; Zhang et al., 2004; Xia et al., 2007; Yan et al., 2008; He et al., 2009; Fan et al., 2010; Cai et al., 2011; Xu et al., 2012; Wu et al., 2012; Zhang et al., 2015; Yu et al., 2016; Deng et al., 2016; Zhuang et al., 2017; etc.) and columnar (e.g., Chiang et al., 2007; Pan et al., 2010; Yu et al., 2011; Zhao et al., 2013; Tao et al., 2014; Zhu et al., 2014; Che et al., 2011; 2013; 2014; 2015a, b, c; Xia et al., 2016; Zheng et al., 2016; Qi et al., 2016, etc.) aerosol optical properties (and DRFs), especially in China. However, surface data cannot completely represent the total conditions of aerosols in the atmosphere as these aerosols are highly affected by the variations in boundary layers. The related deficiency could be solved with measurements of the columnar aerosols. For studies of surface aerosols, people mainly focus on the aerosol absorption coefficient (AAC) and scattering coefficient (SC). For columnar aerosol observations, the detailed aerosol optical and physical properties can be obtained, including the aerosol optical depth (AOD), refractive index, Ångström exponent (AE), etc. Che et al. (2015a) introduced a systematic long-term measurement of the countrywide total AOD and AE in China from 2002 to 2013 and indicated that the annual mean AODs were 0.14, 0.74 and 0.54 for rural sites, urban sites, and eastern China, respectively. There are also some researches focusing on the aerosol optical properties in the YRD (Pan et al., 2010; Yu et al., 2011; Zhuang et al., 2014a; Qi et al., 2016). In addition to the aerosol optical properties, the observation-based aerosol DRFs have also been estimated around the world (such as those found in Markowicz et al., 2008; Khatri et al., 2009;

Kuhlmann and Quaas, 2010; Alam et al., 2011, Zhuang et al., 2014a, and Xia et al., 2016). However, almost all these investigations focused on the total aerosol forcing. For example, Xia et al. (2016) stated that the regional mean aerosol DRF in China was approximately -16~-37 W/m^2 at the TOA and approximately -66~-111 W/m^2 at the surface when the solar zenith angle was approximately 60°.

Although considerable studies of the observed columnar aerosol optical properties have been carried out in China and even within the YRD (one of the regions with the fastest urbanization in China), gaps in the current observations remain, especially in the urban areas of those regions with intensive human activities. In the YRD or eastern China, most of the investigations of the aerosol optical properties have focused on the coastal, lake and rural regions (Pan et al., 2010; Yu et al., 2011; Che et al., 2015a; Qi et al., 2016) of the central to eastern YRD. Additionally, most of these studies address only the total aerosol optical properties (independent of modes and compositions), except for the work of Qi et al. (2016). They also introduced the aerosol physical parameters and size fractional SSA of an eastern coastal city (Hangzhou, hereinafter written as urHZ) of the YRD, which is approximately 300 km away from the western YRD. As implied in Zhang et al. (2012), aerosols have complicated compositions and spatial distributions, especially in rapidly developing regions (such as YRD). Thus, considerable differences might exist in the aerosol optical and physical properties among the sites within the YRD. Additionally, none of research mentioned above studied the aerosol DRFs. Some investigations of the columnar aerosols in the western YRD (urNJ) were carried out by Zhuang et al. (2014a), but significant issues (not considered in their work) still require further study, such as the size fractional optical parameters and the DRFs of different aerosol components, as well as the aerosol physical properties of the different size fractions. Therefore, a more integrated investigation of the aerosol optical and physical properties, as well as their DRFs in the YRD, is still required. In this study,

the unaddressed issues for the western and whole YRD region mentioned above will be studied based on the measurements of a Cimel sun photometer in urNJ combined with a radiation transfer model (TUV, Madronich, 1993). Additionally, the aerosol types and mixings in the region will be further identified and discussed based on the relationships among the aerosol optical properties. Third, the observed aerosol profiles, which have not previously been considered in the YRD, are discussed and used to calculate the aerosol DRFs. The results of this study will be advantageous to further understanding the characteristics of aerosols over the eastern region of China. Additionally, this work will help improve aerosol model performance as well as the modelled climatic effects in the relevant regions. First, the observed aerosol parameters can be used for data assimilation to obtain more accurate inputs (including improved initial conditions and air pollutant emissions) for the model (Jiang et al., 2013 and Peng et al., 2017). Second, more precise aerosol refractive indexes and size distributions used in these numerical models will yield more reasonable aerosol loadings and DRFs (Ma et al., 2017). Third, both the aerosol optical properties and DRFs can be used to validate the simulations.

The methods are described in Section 2. The results and discussions are presented in Section 3, followed by the conclusions in Section 4.

2 Methodologies

2.1 Sampling station and instruments

The observation site (Urban Environmental Monitoring Station of Nanjing University) is located in the downtown area of Nanjing City (hereafter shortened to urNJ; located at 32.05° N, 118.78° E) in the western YRD. The site is on the roof of a 79.3-m-tall building, surrounded by few higher obstacles

and with no industrial pollution sources within a 30 km radius. However, there are several main roads with apparent traffic pollution. Detailed information about the site is available from Zhu et al. (2012).

The columnar aerosol optical properties and physical characteristics of the site were measured by a Cimel sun photometer (CE-318, Holben et al., 1998) during the period from Apr 2011 to Feb 2014. Routine maintenance and calibration was performed during the observational period. Due to malfunctions of the instrument and problems with data transmission, the data from May to Sep 2012 and from Aug to Dec 2013 are invalid and were thus excluded. The wavelength-dependent AOD and AE of the total aerosols were directly measured by CE-318, while the following variables, including the aerosol size distributions; fractionated (fine and coarse) aerosol effective radius (R_{eff}); mean radius (R_{mn}), volume concentrations (Vol); wavelength-dependent optical depths of the various sizes of scattering, absorbing and total aerosols; aerosol SSA; and the wavelength-dependent refractive indices, are derived from the DOBVIC algorithm Version 2 (Dubovik et al., 2000; 2006). This algorithm has been widely used by the Aerosol Robotic Network (AERONET) and the China Aerosol Remote Sensing Network (CARSNET), while the products have been used globally, as introduced in the Introduction, due to their high accuracies. The errors for the AOD, absorption AOD (AAOD) and SSA are 0.01, 0.01 and 0.03, respectively (Yu et al., 2011; Li et al., 2015c). The errors of the fine and coarse aerosol SSAs are 0.037 and 0.085, respectively (Xu, 2015). The errors of the refractive index are 0.04 for the real part and 0.0025-0.0042 for the imaginary part (Yu et al., 2011). Additionally, the error of the volume size distribution is less than 10% in the peak regions but is approximately 35% in valley or interval regions for the fine and coarse modes (Yu et al., 2011). Detailed descriptions of CE-318 and the corresponding observations from CARSNET are available from Li et al. (2015a) and Che et al. (2015a). For comparison, the 550 nm AODs and SSAs are calculated based on the given AODs at other

157 wavelengths and AEs (Angstrom. 1929):

158 $$AOD_{550nm} = AOD_{440nm} \times (\frac{550_{nm}}{440_{nm}})^{-AE_{440/870nm}} \quad (1)$$

159 $$AAOD_{550nm} = AAOD_{440nm} \times (\frac{550_{nm}}{440_{nm}})^{-AAE_{440/870nm}} \quad (2)$$

160 $$SSA_{550nm} = \frac{AOD_{550nm} - AAOD_{550nm}}{AOD_{550nm}}. \quad (3)$$

161 For a further comparison, concurrent observations of the surface total AAC and AE measured by a
162 7-channel Aethalometer (model AE-31, Magee Scientific, USA, Hansen et al., 1984; Weingartner et al.,
163 2003 and Arnott et al., 2005) are used. The detailed calculations and corrections of the AAC at the site
164 were presented by Zhuang et al. (2015). Additionally, the monthly mean AOD and AE of the total
165 aerosols from the satellite-based Moderate Resolution Imaging Spectroradiometer (MODIS) were used
166 in the analysis.

167 Based on the observed wavelength-dependent aerosol optical properties, the DRF of the aerosols
168 in urNJ is investigated using the radiation transfer model TUV (Madronich, 1993). Only clear-sky
169 DRFs are addressed here because almost all the measurements are carried out in free sky conditions.
170 The solar component of the radiative transfer scheme in the TUV model follows the δ-Eddington
171 approximation. In addition to the aerosol optical properties, the surface albedo (Palancar and Toselli,
172 2004) and aerosol vertical profiles (Forster et al., 2007) might also have significant influences on the
173 DRF. Thus, the wavelength-dependent surface albedo from MODIS, the annual and seasonal mean
174 aerosol profiles from the Cloud-Aerosol Lidar and Infrared Pathfinder Satellite Observations
175 (CALIPSO) and the Polarization-Raman Lidar (PRL) in Nanjing are included when assessing the
176 aerosol DRF. The aerosol DRF in this study is defined as the difference in the net shortwave radiative
177 fluxes when including or excluding the aerosol effects at the TOA and surface. The gas absorptions in

178 the atmosphere were set to be constant. The scattering aerosol SSA was set to 0.9999 (similar to that of
179 sulfate or nitrate, Li et al., 2015b) when calculating its DRF. The DRF of the absorbing aerosols is
180 derived from the differences between the total and scattering aerosol DRFs.
181
182 **3 Results and discussions**
183 **3.1 Optical properties of the aerosols**
184 Unless otherwise specified, the AODs, SSAs and refractive indices of the aerosols hereinafter all
185 represent the ones at 550, 550 and 440 nm, respectively. In addition to the total aerosols, the
186 size-dependent (i.e., the fine and coarse fractions) aerosol optical properties of the different types
187 (scattering and absorbing aerosols) are also discussed in this section. Therefore, there are nine types of
188 aerosols: total aerosols (TA), total fine aerosols (FA), total coarse aerosols (CA), scattering aerosols
189 (SA), fine scattering aerosols (FSA), coarse scattering aerosols (CSA), absorbing aerosols (AA), fine
190 absorbing aerosols (FAA), and coarse absorbing aerosols (CAA).
191 Table 1 summarizes the statistics of the aerosol optical properties during the study period in urNJ.
192 The mean total aerosol AOD is 0.65, and the SA's account for as much as 93.8% of this category. Fine
193 mode AOD (FAOD), fine mode scattering AOD (FSAOD) and fine mode absorbing AOD (FAAOD)
194 account for 81.53%, 81.97% and 56.09% of the total AODs, scattering AODs (SAODs) and absorbing
195 AODs (AAODs), respectively, implying that coarse aerosols absorb more than fine ones. The 440/870
196 nm AE of the total, scattering and absorbing aerosols are approximately 1.20, 1.19, and 1.32,
197 respectively. Fine aerosols have much higher AEs, which can be 0.4-0.5 greater than those of the total
198 aerosols. Overall, the absorbing aerosols have smaller sizes than the scattering ones in all modes,
199 especially in the coarse mode, which is consistent with the results from the surface aerosols at the site

200 (Zhuang et al., 2017). The mean SSA of TA, FA and CA is 0.93, 0.95 and 0.82, respectively, further
201 implying that the coarse aerosols have different compositions than the fine aerosols. The comparisons
202 also indicate that surface aerosols (SSA=0.9 in Zhuang et al., 2017) are slightly more absorptive than
203 the columnar aerosols in urNJ. The mean 440 nm refractive index is approximately 1.44+0.0084i.
204 Table 1
205
206 **3.1.1 Seasonal variations in the aerosol optical properties**
207 Figure 1 presents the monthly variations in the AOD (a), SAOD (b) and AAOD (c) as well as the
208 contributions of their fine and coarse modes to their corresponding totals. The temporal variations in
209 the total aerosol AOD are consistent with those of SAOD due to the significantly large ratio of
210 SAOD/AOD. The AODs are all considerably high in the winter due to the more intense emissions of
211 trace gases and particles (Zhang et al., 2009). Additionally, they are also high in spring and summer
212 under the influences of dust, high efficiencies of moisture absorption growth and chemical
213 transformation (Li et al., 2015a). Therefore, the seasonal variations of the total AODs are not so
214 obvious in urNJ in the western YRD. These influences are prominent in the AOD seasonality for
215 different aerosol types within the different size segments. The largest AODs appear in the spring for the
216 coarse aerosols, whereas they appear in the summer for the fine aerosols in urNJ. The figure also
217 implies that the scattering aerosols might have different size distributions than the absorbing aerosols.
218 The fine mode fraction is 0.83 (peaking at 0.97) for scattering aerosols and is 0.56 (peaking at 0.83) for
219 absorbing aerosols. It's noting that AOD in August does not include the ones in 2012 and 2013.
220 Coincidentally, air pollution has been controlled since 2012 in Nanjing due to hosting international
221 events in Aug 2013 and 2014. August AOD in 2011 is 1.18, much higher than those in 2012 (0.75) and

2013 (0.63) as referred from the MODIS retrievals. As a result, the AOD in August shown in Figure 1 is "unusually" high.

Figure 1

The aerosol AEs also have substantial seasonal variations, especially for the absorbing aerosols, as illustrated in Figure 2. The seasonal variation of the fine aerosol AE is highly consistent with the coarse one for the absorbing aerosols while it is opposite for the scattering aerosols. Nevertheless, all AEs in the summer are the closest to 0 possibly due to the effects of high RH (Zhuang et al., 2014a). The whole mode AE of each aerosol type is determined by the both variations in the AEs in each mode and the fine mode fraction. Therefore, the smallest AEs appear in the summer (0.74 in July) for the total absorbing aerosols but appear in the spring (0.94 in Mar) for the total scattering aerosols. Similarly, the total aerosol AE is determined by both the variations of each aerosol type's AE and the ratio of the scattering (or absorbing) aerosols to the total. And the seasonality of the total aerosol AEs is more consistent with that of the scattering aerosols. The figure also indicates that the scattering aerosols have much larger sizes than the absorbing aerosols, especially those in the coarse mode. Further comparisons indicate that the seasonal variations of the columnar SAE and AAE are consistent with their surface ones (Zhuang et al., 2017) at the site.

Figure 2

In addition to AOD and AE, the monthly variations in the aerosol SSAs and refractive indices are

244 also investigated, as shown in Figure 3. SSA is affected by both scattering and absorbing aerosols, as
245 well as their relative contributions. The fine particles have much stronger scatterings than the coarse
246 aerosols. Their SSAs have relatively weaker seasonality. Overall, both FSSA and CSSA are relatively
247 smaller in the warmer seasons, although they were considerably large in August 2011. The total aerosol
248 SSA is somewhere between the FSSA and CSSA and depends on the ratios of the FAOD to AOD. Thus,
249 these SSAs have different seasonal variations from the FSSA or CSSA. SSA is also rather small in
250 spring due to the largest contribution of coarse aerosols occurring in this season. The aerosol refractive
251 indices also show considerable seasonality. The real part is large in the spring but small in the summer,
252 which is similar to what was observed in Taihu Lake in the central YRD (Yu et al. 2011). The
253 imaginary parts show relatively weaker seasonal variations than the real parts.
254
255 Figure 3
256
257 To provide a more quantitative knowledge, Table 2 summarizes the abovementioned seasonal
258 means with the corresponding standard deviations for all the aerosol optical properties. And it's more
259 obviously reflecting the different variations of the optical properties among different aerosol categories.
260 For example, CAOD, CSAOD, CAAOD account for the majority of the AOD, SAOD and AAOD in
261 the spring, with ratios of 30.1%, 27.9%, and 58.1%, respectively. FAOD, FSAOD, FAAOD account for
262 the majority of the AOD, SAOD and AAOD in the summer, with ratios of 90.5%, 91.2% and 70.2%,
263 respectively. Comparisons indicate that the seasonal variations of the optical properties are highly
264 spatially inhomogeneous within the YRD. As indicated by Che et al. (2015a) and Qi et al. (2016), the
265 largest AOD was found in the spring, while the lowest one appeared in the summer in urHZ, another

266 city on the eastern coast of the YRD. In Taihu Lake, a rural site in the central YRD, the lowest AOD
267 appeared in the winter (Pan et al., 2010; Yu et al., 2011). Additionally, the aerosols absorb the most in
268 the winter in the central regions of the YRD (Taihu Lake and urHZ), and their SSAs are as small as
269 0.88 (Yu et al., 2011 and Qi et al., 2016). The aerosols in the western YRD (urNJ) are more scattering
270 than those of the preceding areas. Nevertheless, AE variations are more consistent with each other
271 between these sites, being smallest in the spring and largest in the fall.

272 Table 2

273

274 **3.1.2 Frequencies of the aerosol optical properties**

275 All AODs and SSAs follow a near lognormal pattern, and almost all the AEs and refractive
276 indices follow a unimodal pattern (Figure 4). The ranges around their means are dominant, accounting
277 for at least 60% of the total data samples during the entire study period. Similar to the temporal
278 variations, the frequency distributions of the total aerosols (not shown) are also highly similar to those
279 of the scattering aerosols in both the fine and coarse modes. The frequencies of the absorbing aerosol
280 AEs differ from those of the scattering aerosol AEs. The occurrences of smaller CAAE (or large FAAE,
281 AAE) values are also relatively high. Due to different absorbed fractions among coarse, fine and total
282 aerosols, the curve of CSSA (FSSA) has a leftward (rightward) shifting compared with that of SSA,
283 peaking around 0.84 (0.97). The fine aerosol SSAs were concentrated in a more narrow range (~0.1)
284 than the CSSAs were (~0.3). For the refractive index, the frequencies peak around 1.42 and 0.008 for
285 the real and imaginary parts, respectively, in urNJ during the study period. The frequency patterns of
286 the aerosol optical properties also have substantial seasonality (not shown here). Overall, the curves
287 shift leftward in low value seasons and rightward in high value seasons. In the summer, the AOD

288 curves might even have two peaks for the scattering or total aerosols, which are similar to the
289 observations in Taihu Lake (Yu et al., 2011).
290
291 **3.1.3 Comparisons with MODIS AOD, AE and surface aerosols**
292 The AOD and AE observed by CE-318, to degrees, are well correlative with those from MODIS in
293 terms of their seasonal variations and magnitudes (Figure 5). The linear correlation coefficients are
294 0.71 and 0.67 between the monthly mean CE-318 and MODIS AODs and between the monthly mean
295 CE-318 and MODIS AEs, respectively. The AOD from MODIS is greater (~1.2 times) than that from
296 CE-318, with an average value of 0.80 during the study period. The slop of the linear fitting is 1.12 for
297 AOD in urNJ, similarly to that in central China (slope=1.16, Dong et al., 2013). The mean AE at
298 412/470 nm from MODIS is approximately 1.42. The standard deviations of the AOD and AE values
299 are much larger for CE-318 than for MODIS, possibly due to the higher temporal resolution of the
300 CE-318 observations.
301
302 Figure 5
303
304 The columnar AAOD and AAE values from CE-318 are less related to the surface aerosol
305 absorption coefficient (AAC) and AAE from AE-31 (Figure 6). Because surface aerosols are mainly
306 affected by local and regional emissions, and their loadings are highly related to the degrees of
307 boundary layer development (Zhuang et al., 2014b and 2015). The columnar AAODs could be further
308 affected by emissions and transports in the upper atmosphere. The surface AAE is concentrated in a
309 narrower range and is larger (1.6) than that from CE-318. The linear correlation coefficients between

310 the AAOD and AAC and between the columnar and surface AAEs are 0.39 and 0.41, respectively,
311 which are slightly worse than those between FAAOD and AAC (0.46) and between the columnar
312 FAAE and surface AAE (0.47).
313
314 Figure 6
315
316 **3.1.4 Brief discussions**
317 Results here allow us to better understand the characteristics of the aerosols in the YRD. And they
318 might be also useful for improving aerosol model performances and their radiative effects in the YRD
319 or eastern China as referred in Introduction.
320 Most studies of the aerosol optical properties in China mainly focus on the AOD and AE of the
321 short-term total aerosols (i.e., episodes, Che et al., 2013; Zheng et al., 2016; Che et al., 2015b),
322 although the annual (Yu et al., 2011) and decadal (Che et al., 2015a) scale aerosols have been also
323 carried out in recent years based on CE-318 measurements. Results here show that the mean AOD in
324 urNJ is greater than those in northern China and the PRD but is smaller than those of the coastal cities
325 of the YRD. The AE is larger in urNJ than in northern and central China. Che et al. (2015a) further
326 suggested that those aerosols in urban areas likely had larger AODs and AEs than those in mountain
327 and desert areas. It's the same in urNJ. Qi et al. (2016) showed that the aerosol SSAs at 440 nm in
328 urHZ are approximately 0.90, 0.92 and 0.70 for the total, fine and coarse aerosols, respectively, also
329 implying that the coarse aerosols absorb more than the fine ones. Our measurements show similar
330 results. However, the aerosols in urNJ scatter more than those in urHZ in both the fine and coarse
331 modes, also revealing the inhomogeneous distributions of the aerosol compositions in the YRD. This

study further augments the current observations of the aerosol optical properties in the YRD compared with previous studies.

3.2 Physical properties of the aerosols

In addition to the optical properties, the aerosol physical properties, including the volume size distributions, mode-dependent sizes (radius) and volume concentrations, were also retrieved. Figure 7 shows the volume size distributions of the aerosols in different seasons (Figure 7a) and at different AOD (or polluted) levels (Figure 7b) in urNJ. It shows that the aerosols in urNJ have a typical bimodal structure in their volume size distributions in all seasons, presenting two-mode lognormal distributions in both the fine (radius < 0.6 μm) and coarse modes (radius > 0.6 μm). Their annual peaks appear at radii of 0.148 μm for the fine mode and 2.94 μm for the coarse mode. The aerosol volume size distributions also have substantial seasonality. Dust episodes lead to the peak values in the spring being much smaller in the fine mode than those in the coarse mode, which is the opposite trend than in the other seasons (especially in the summer). Therefore, the mean radius of the aerosols increases significantly in the spring due to the high proportion of coarse particles, leading to a smaller AE, as discussed in the previous sections. In the summer, the curve has a rightward shift, showing a larger aerosol size in both the fine and coarse modes due to the high hygroscopic growth efficiency. The fine particles are dominant in the summer and result in large AE values, opposite to the patterns in the spring. The aerosol volume size distribution varies with different AOD values (Figure 7b) in urNJ. Overall, the peak value has a substantial rightward shift with increasing AOD for fine aerosols while a slightly leftward shift for coarse aerosols, implying that the growth of the fine aerosols is advantageous to enhance the aerosol radiative effect. In urNJ, both fine and coarse particles have approximately the

same levels when AOD is below ~0.8. In addition, the fine aerosols begin to dominate more when AOD>0.8. The results here are mostly consistent with the ones from Yu et al. (2011), Qi et al. (2016), and Zheng et al. (2016). However, the figure here further indicates that both fine and coarse particles themselves might cause very serious haze pollutions in YRD, showing considerably high peak values in both fine and coarse modes, which has not been observed in previous publications. The aerosol size distributions here are also very useful for optimizing numerical models.

Figure 7

To further investigate the physical features, the seasonal variations in the aerosol effective and mean radius and the volume concentrations in urNJ are presented in Figure 8. The mean effective radius, which is generally smaller than the mean one in all modes, is approximately 0.34, 0.16, and 2.18 μm for the total, fine and coarse aerosols, respectively, during the study period. The seasonal variations in the radii have a strong anti-correlation to that of the AEs (Figure 2). Both the fine and coarse aerosol radii are larger in the summer than in the other seasons while the total aerosol radius is much larger in the spring. Unlike the radius, the seasonal variations in the volume concentrations of the fine and coarse aerosols are different, peaking in the spring for coarse aerosols and in the summer for fine aerosols. Although both the fine and coarse aerosols have the same annual volume levels in urNJ, their contributions to the total aerosol volumes vary significantly with season. The coarse aerosols lead directly to the largest total aerosol volume peaking in the spring.

Figure 8

3.3 Aerosol classification based on optical properties

The aerosol clusters, to a certain degree, can be identified based on the relationships between SSAs at 491 nm and AEs at 491/870 nm, between the real refractive index (RRI) at 670 nm and the AE at 491/870 nm, and between the SSA differences ($dSSA=SSA_{870nm}-SSA_{491nm}$) and AE at 491/870 nm, as presented by Russell et al. (2014). They proposed a Mahalanobis Classification based on "a priori" information for each type of aerosol source (e.g., dust, urban, biomass aerosols). Different aerosols would then be mostly concentrated within the corresponding ellipses of a two-dimensional scatter plot of SSA versus AE (or RRI versus AE, or dSSA versus AE). Based on their classifications, aerosols from pure dust, polluted dust, biomass burning, industrial urban, developing urban, and marine sources (Figure 8 in Russell et al., 2014) can be identified. For example, the polluted dust aerosols are mostly within the ellipses with smaller AE (near 1.0) values, relatively small SSA levels (0.85 to 0.95), and much larger real refractive indices (1.45 to 1.55) and SSA differences (0 to 0.05) than those present for other aerosols. The aerosols from a developing urban area generally have smaller sizes than polluted dust (AE ranging from 1 to 1.6), but they have larger SSA (0.9 to 1.0) values, smaller real refractive indices (1.4 to 1.5) and smaller SSA differences (approximately 0). More classifications can be found in (Russell et al., 2014). Based on their classification standards, the aerosols in urNJ could be basically identified as clusters of polluted dust, developing urban and industrial urban during the sampling period, as shown in Figure 9, which further supports the analysis in Section 3. Although urNJ is only approximately 300-400 km away from the East China Sea, few marine or sea salt aerosol components are observed, as illustrated in Figure 9. Unfortunately, the observations missed a biomass burning event in Jun 2012 (Zhuang et al., 2014b, 2015) because the instrument was having maintenance performed.

Otherwise, the figure would be more comprehensive. Analysis here might help us understand the aerosol sources, transformations, transports and radiative effects in the YRD. In addition, this information also indicates that the Mahalanobis Classification is a very useful approach for classifying aerosol into types, especially in cases of data shortages or insufficient methods. However, this method still has a limitation. The classified ellipses have some overlaps among different aerosols clusters. In overlap regions, classifying the aerosols into types is a challenge. For example, it is not easy to distinguish between polluted dust aerosols with large AE values and urban aerosols with smaller AE. Therefore, if there are two kinds of aerosols with nearly identical coordinates, further information is needed, or a more effective approach should be taken into account.

Figure 9

In addition to the types, the aerosol mixtures/compositions can also be identified based on SSA and AAOD. Generally, dust aerosols have strong absorption in the ultraviolet (UV) band but become non-absorbing in the visible band, leading to SSAs increasing monotonically with the wavelength. For biomass burning aerosols, the SSAs decrease monotonically with wavelength. Non-monotonic variations in SSA with changes in wavelength might be due to aerosol mixtures dominated by another type of aerosol, as indicated by Li et al. (2015c). They proposed two curvature parameters to provide additional information on the aerosol compositions: the second derivative of the second-order polynomial fit of the SSA and wavelength and the fit of the AAOD and wavelength, as shown in Eq. 4 and Eq. 5.

$$\ln(SSA_\lambda) = \beta_2 \ln(\lambda)^2 + \beta_1 \ln(\lambda) + \beta_0 \quad (4)$$

$$\ln(AAOD_{\lambda}) = \alpha_2 \ln(\lambda)^2 + \alpha_1 \ln(\lambda) + \alpha_0 \quad (5)$$

where $-\beta_2$ and α_2 are the SSA curvature and AADO curvature, respectively. Detailed descriptions were presented by Li et al. (2015c). Based on these parameters, the aerosols can be identified as dust dominated, BC (including biomass burning and urban/industrial aerosols) dominated and other mixed (peak) type aerosols because the curvature probability (or frequency) distributions are different for the different aerosol mixtures. As indicated in Li et al. (2015c), the SSA or AAOD curvature is mostly concentrated at approximately 0 for the BC-dominated aerosol mixture, which is much smaller than that of the dust-dominated aerosol mixtures (0.1 for SSA curvature and 0.5-1 for AAOD curvature) over East Asia. Based on their method, the curvatures of SSA and AAOD are calculated and then divided into three categories according to the monotonicity of the SSA. The results show that there are approximately 15.0%, 27.5% and 42.3% occurrences of monotonically increasing, decreasing and 670 nm peaking SSA spectra, respectively, in urNJ. In addition, their probability (or frequency) distributions are plotted in Figure 10. The figure indicates that the SSA and AAOD curvature patterns are highly consistent with those in Li et al. (2015c) for the monotonic categories, which implies that the ~15% and ~27% samples with monotonically increasing and decreasing SSA spectra are the dust-dominated and BC-dominated mixing aerosols, respectively, in urNJ during the observed period. For example, a very strong dust storm from northwest China and Mongolia on 1st May 2011 (Li et al., 2015a) directly yielded mean SSA and AAOD curvatures of 0.12 and 1.11, respectively, which are close to the values (0.11 and 1.24, respectively) of the pure dust aerosols (Li et al., 2015c). For the rest of the categories with non-monotonic SSA spectra, the SSA curvatures are mostly concentrated from 0.3 to 0.8, implying that the dust component might not exceed 10%, while the scattering species (organic carbon not included) accounted for at least 30% of the mixing particles in western YRD

442 according to the sensitivity results from Li et al. (2015c). Additional data are needed to derive further
443 information. However, these results might help us gain a better understanding of the mixings of
444 aerosols in the urban areas of the YRD. Similar to Russell et al. (2014), Li et al. (2015c) provided an
445 effective approach for classifying the aerosol compositions based on a single data set (such as the
446 CE-318 retrievals).
447
448 Figure 10
449
450 **3.4 The direct radiative forcing of the aerosols**
451 Based on the abovementioned wavelength-dependent optical properties combined with the
452 observed surface albedo and aerosol profiles, the clear-sky size-dependent aerosol DRF of the fine and
453 course components at both the TOA and the surface in urNJ are investigated using the radiation transfer
454 model TUV (Madronich, 1993). Due to a lack of SSA observations of each aerosol component, the
455 scattering aerosol DRF is estimated based on a given SSA value (0.9999, equal to that of sulfate or
456 nitrate aerosol) in a reference (Li et al., 2015b). As indicated in the last section, the absorbing aerosols
457 in urNJ are always in a mixed state. Therefore, the absorbing aerosol DRF cannot be estimated directly
458 using the BC SSA. Here, this value is derived from the difference between the total and scattering
459 aerosol DRFs, which might be more representative. For comparison, the aerosol DRF is also calculated
460 based on the AAODs, AAEs and BC SSA (Li et al., 2015b).
461 Observational aerosol profiles, which have not have been used in previous investigations (e.g.,
462 Zhuang et al., 2014a), might be important to the DRF estimations. Figure 11 shows the mean vertical
463 aerosol profiles observed by CALIPSO (annual scale data) and the PRL (seasonal scale data) in

Nanjing. For further comparisons, all the profiles in the figure were standardized to percentages (%). The figure suggests that the ground and satellite-based aerosol profiles are substantially different. The CALIPSO profile is more homogeneous than the PRL one, accounting for approximately 61% and 88%, respectively, below 4 km. Due to the lack of the long-term measurement of PRL and the different products of the different observational platforms, both the CALIPSO and PRL profiles are used here. Additionally, a combined profile (grey line) of the averaged CALIPSO and PRL values is included and indicates that aerosols account for approximately 75% of the total below 4 km and approximately 60% in the boundary layer for the combined profile, which is somewhat similar to the default profile of TUV (Palancar and Toselli, 2004). All these four profiles were used when estimating the aerosol DRFs.

Figure 11

3.4.1 The aerosol direct radiative forcing in clear-sky conditions

Hereinafter, DRFs, unless otherwise specified, represent the averaged values from CALIPSO, PRL and a combined profile-based forcing in clear-sky conditions. Figure 12 shows the seasonal variations in the size-dependent daytime TOA and surface DRFs of the total, scattering and absorbing aerosols in urNJ. The aerosol DRFs are highly dependent on the aerosol optical properties and compositions. Overall, the fine aerosols contribute considerably more to the total aerosol DRFs, especially for scattering aerosols. The coarse aerosol DRF accounts for only 13.3% for the scattering aerosols, while this fraction is >33.7% for the absorbing aerosols at both the TOA and surface in urNJ. Negative scattering aerosol DRFs could be significantly offset at the TOA and could be further strengthened at the surface by absorbing aerosols. Therefore, the total coarse aerosol DRF at the TOA

is very weak due to a much smaller CSSA and subsequently accounts for a much smaller contribution to the total aerosol DRF than the fine aerosols do. Both the scattering and absorbing aerosol DRFs have similar seasonality to their AODs. And the scattering aerosol DRFs have the same seasonality as the absorbing ones within the same mode. In addition to AODs, the surface albedo and solar zenith angle also have a strong influence on the variations in the aerosol DRFs. As implied by Zhuang et al. (2014a), a brighter surface would yield a weaker negative DRF and a stronger positive DRF, assuming a fixed AOD. The seasonal mean surface albedo averaged from four wavelengths (440, 670, 870 and 1020 nm) is approximately 0.145, 0.170, 0.129, and 0.137 in the spring, summer, fall, and winter, respectively. As a result, the scattering and fine absorbing aerosol DRFs are also strong in the winter and spring, respectively. Unlike those of the single aerosol types, the variations of the total aerosol DRFs are co-affected by those of both the scattering and absorbing aerosols. Thus, the strongest TOA DRF of the total fine aerosols appears in the winter instead of the summer, and the total coarse aerosol DRFs are positive at the TOA in the summer. For all modes, the seasonal variations of the total aerosol DRFs at the TOA are more consistent with those of the fine mode. Different from the TOA DRFs of the total aerosols, the surface DRFs are much more consistent with those of the corresponding AODs.

Figure 12

For further comparisons (Figure 13), the absorbing aerosol DRFs based on the observed AAOD, AAE and fresh BC SSA (Li et al., 2015b) are also used. Although the absorbing aerosol DRFs are estimated in different ways, they are highly correlated at both the TOA and surface, as shown in the figure. Apparently, the DRFs from the second method are much weaker than those from the first

508 calculation, possibly due to the absorbing aerosols in urNJ being in a constantly mixed state, as shown
509 by the analysis in the previous section and as indicated by Zhuang et al. (2015). Jacobson (2000)
510 suggested that the aged (mixed) absorbing aerosols have a much stronger ability to absorb solar
511 radiation, by a factor of two. Zhuang et al. (2013a and 2013b) stated that the simulated regional mean
512 TOA DRF of the mixed BC (+1.56 W/m^2) over East Asia is approximately 1.9 times that of the
513 unmixed BC. The ratio is approximately 1.73 in this study, implying that the absorbing aerosol DRF
514 from the first method is reasonable. The comparison here further proves the importance of the mixing
515 states in estimating the absorbing aerosol radiative effects.
516
517 Figure 13
518
519 Table 3 lists the annual mean size-dependent DRFs of the total, scattering and absorbing aerosols
520 at both the TOA and the surface in urNJ. The DRFs at the surface are all stronger than those at the TOA.
521 The mean DRFs are -10.69, -16.45, 5.76 W/m^2 at the TOA and -25.54, -21.37 and -8.38 W/m^2 at the
522 surface for the TA, SA and AA, respectively. The fine mode TOA DRFs are nearly an order of
523 magnitude stronger than those of the coarse mode for the total and scattering aerosols. The DRFs of the
524 fine absorbing aerosols have the same order of magnitude but are stronger than those of the coarse
525 absorbing aerosols. It's noting that the total DRFs in the table are not exactly the sum of the
526 contributions from the fine and coarse ones, because the coarse aerosol affection on the solar radiation
527 is excluded when calculating the fine aerosol DRF separately, and vice versa.
528 Table 3
529

Various studies of aerosol DRFs have been carried out based on observations or numerical models. Overall, the DRFs of urban aerosols are much stronger than those on regional or global scales. Forster et al. (2007) summarized the global mean clear-sky DRFs of the total observational aerosols as -5.4 W/m^2. Zhuang et al. (2013a and 2013b) indicated that simulated clear-sky DRFs are -4.97 W/m^2 for total aerosols and +1.2 W/m^2 for BC over East Asia. On a subregional or urban scale, the observation-based analysis showed that the total aerosol DRFs always exceeded 10^1 W/m^2 (Markowicz et al., 2008; Khatri et al., 2009; Wang et al., 2009; Kuhlmann and Quaas, 2010; Alam et al., 2011; Che et al., 2015c, and so on). For example, the total aerosol DRF could be as strong as -25 W/m^2over the Qinghai-Tibet Plateau (Kuhlmann and Quaas, 2010) and -30 W/m^2 in the north China Plain (Che et al., 2014 and 2015c). Our results show that the aerosols in the urban area of the western YRD could also exert very strong DRFs, reaching as high as -25.5 W/m^2 at the surface. Apparently, the DRFs here have smaller uncertainties than those from simulations because of the use of observations. And they might be also more precise compared with previous estimation in Zhuang et al. (2014a). This study further investigated the size fractional DRFs of different aerosol components in urban areas of the western YRD, which allows a better understanding of the effects of aerosols on solar shortwave radiation. In addition, these issues have not been addressed in previous studies. The results here can also be used to validate numerical simulations and to evaluate model performance concerning aerosol radiative effects.

3.4.2 Sensitivity of the aerosol direct radiative forcing to aerosol profiles

Different aerosol profiles might result in different DRFs. Figure 14 presents the TOA and surface DRFs of different aerosol types, including the SA, AA and TA, based on four kinds of aerosol profiles from CALIPSO, PRL, the combined CALIPSO and PRL shown in Figure 11 and the default one from

552 TUV (Palancar and Toselli, 2004) in clear-sky conditions. The figure shows that the aerosol DRFs in
553 clear-sky conditions are not very sensitive to the aerosol profile, although the absorbing aerosol TOA
554 DRFs are more sensitive than those of the scattering aerosols. Overall, both the scattering and
555 absorbing aerosol DRFs at the TOA become weaker to some extent when more aerosols are
556 concentrated in the lower layers of the atmosphere, especially for the AA's. Here, a profile impact
557 factor (PIF) is defined as the ratio of the standard deviations among the four types of DRFs in Figure
558 14 to the averaged values of these four DRFs. The PIF is approximately 4.97% for the absorbing
559 aerosol TOA DRF and is below 2% for the rest of the types of DRFs. In contrast, the aerosol profiles
560 might have much stronger influences on the DRFs in cloudy sky conditions because the absorbing
561 aerosols over brighter cloud will absorb more shortwave radiation (Podgorny and Ramanathan, 2001).
562 This issue will be addressed in the future.
563
564 Figure 14
565
566 **3.4.3 Brief discussions**
567 Although the observation-based DRFs of the total, scattering and absorbing aerosols as well as
568 their sensitivities to the aerosol profiles are analysed in this study, uncertainties still exist due to the
569 measurement errors of the optical properties mentioned in Section 2. Additional estimations of the
570 aerosol DRFs are carried out based on the errors of AOD, AAOD and SSAs. The results indicate that
571 the greater uncertainties of the aerosol DRFs are mainly derived from the errors of SSA or AAOD. The
572 uncertainty of the total aerosol AODs (0.01) yield only approximately 1% relative biases for the total
573 aerosol DRFs at both the TOA and surface. The total or fine aerosol SSA errors (0.03 or 0.037,

574 respectively) may result in approximately 24% of the uncertainties at the TOA (<15% at the surface)
575 for the corresponding DRFs. A larger coarse aerosol SSA error (0.085) leads to an ~24% uncertainty of
576 its surface DRFs. AAOD errors (0.01) cause approximately 20% of the uncertainties for the absorbing
577 DRFs at both the TOA and surface while accounting for only 1.2% of the scattering DRFs uncertainties.
578 Overall, these uncertainties are smaller than those presented in the 5th IPCC report (IPCC, 2013) and
579 could be further decreased if the measurements or the algorithms were fairly improved. For example,
580 the absorbing aerosol DRFs would become more accurate if corresponding SSAs could be obtained by
581 measurements. Also, the aerosol DRFs would be better estimated to a degree if its profiles with higher
582 temporal resolution could be used in future. Additionally, extremely high aerosol loadings are
583 frequently observed during serious pollution episodes, including dust storms, biomass burning, and
584 regional transport (Zhuang et al., 2014a, b and 2015). The aerosol optical and physical properties as
585 well as the radiative forcing are different during these extreme episodes, which also deserves further
586 study.
587
588 **4 Conclusions**
589 In this study, the size-dependent aerosol optical and physical properties observed by a Cimel sun
590 photometer (CE-318), as well as the corresponding DRFs calculated by the radiation transfer model
591 TUV based on observations from the urban area of Nanjing (urNJ), western YRD, are investigated.
592 In the urban area of the western YRD, the annual mean total aerosol AOD is 0.65 and is mostly
593 due to the contribution of the scattering components (0.61). The absorption fraction is as small as
594 ~6.7%. Approximately 80% of the aerosols in urNJ during the sampling period are fine mode aerosols.
595 The absorption fraction is approximately 4.6% in the fine mode and 15.5% in the coarse mode,

596 showing the very different compositions and absorption characteristics of these two kinds of aerosols.
597 Compared with the satellite retrievals, the observations show aerosol optical properties with much
598 higher temporal resolutions and more products. Further analysis of the aerosol optical properties
599 indicates that there might be approximately 15% and 27% occurrences of dust-dominated and
600 BC-dominated mixing aerosols, respectively, in the western YRD during the study period.

601 The aerosols in the western YRD have a two-mode lognormal pattern in their volume size
602 distribution, peaking at the radii of 0.148 and 2.94 μm on an annual scale. The fine particles have the
603 same contribution as the coarse ones when AOD<0.8, and they become predominate when
604 0.8<AOD<1.4. Different from observations in other regions, the results here further reveal that the
605 coarse aerosols might also induce very serious pollution episodes in the YRD. Both fine and coarse
606 aerosols have the same levels of volume concentrations, although their radii differ by an order of
607 magnitude.

608 Similar to AODs, the total fine aerosol DRF also have a much contribution to the totals, especially
609 at TOA (>97%), with a value of -11.17 W/m^2. However, differences exist. For each aerosol type, the
610 coarse aerosol DRF accounts for only ~13.3% for the scattering aerosols while at least 33.7% for the
611 absorbing aerosols at both the TOA and the surface in urNJ. The DRFs estimated for urNJ in this study
612 are much stronger than their regional or global means.

613 Most of the size-dependent aerosol optical and physical properties as well as their DRFs have
614 significant seasonality in the western YRD. The DRF variations for each aerosol type within the same
615 mode are mostly consistent with the variations in the corresponding AODs, peaking in the summer for
616 the fine aerosols and in the spring for the coarse ones. However, the variations in the total aerosol
617 DRFs at the TOA are different from the corresponding AODs because the negative DRFs of the

scattering aerosols are always offset by the absorbing aerosols. Both the fine and coarse aerosols have the largest sizes in the summer, which differs from the total aerosol mode (which peaks in the spring).

The sensitivities of clear-sky aerosol DRFs to the aerosol profiles are not significant and are all smaller than 5%. Overall, both the scattering and absorbing aerosol DRFs at the TOA would become somewhat weaker if more aerosols were concentrated in the lower layers of the atmosphere, especially for the absorbed DRF. Further investigation suggests that another uncertainty of the DRFs is from the measuring errors of the aerosol optical properties. The larger biases are mainly derived from the errors of the SSA and AAOD.

Acknowledgements: This work was supported by the National Key R&D Program of China (2017YFC0209803, 2014CB441203, 2016YFC0203303), the National Natural Science Foundation of China (41675143, 91544230, 41621005), and a project Funded by the Priority Academic Program Development of the Jiangsu Higher Education Institutions (PAPD). The authors would like to thank all members in the AERC of Nanjing University for maintaining instruments, and also thank the anonymous reviewers for their constructive and valuable comments on this paper.

5 References

Alam, K., Trautmann, T., and Blaschke, T.: Aerosol optical properties and radiative forcing over mega-city Karachi. Atmos. Res. 101, 773-782, 2011.

Angström, A.: On the atmospheric transmission of sun radiation and on dust in the air, Geogr. Ann., 11, 156–166, 1929.

Arnott, W. P., Hamasha, K., Moosmuller, H., Sheridan, P. J., and Ogren, J. A.: Towards aerosol

light-absorption measurements with a 7-wavelength aethalometer: evaluation with a photoacoustic instrument and 3-wavelength nephelometer, Aerosol Sci. Tech., 39, 17–29, doi:10.1080/027868290901972, 2005.

Bellouin, N., Boucher, O., Tanré, D., and Dubovik, O.: Aerosol absorption over the clear-sky oceans deduced from POLDER-1 and AERONET observations, Geophys. Res. Lett., 30, 1748, doi:10.1029/2003GL017121, 2003.

Bergin, M. H., Cass, G. R., Xu, J., Fang, C., Zeng, L., Yu, T., Salmon, L. G., Kiang, C. S., Tang, X. Y., Zhang, Y. H., and Chameides, W. L.: Aerosol radiative, physical, and chemical properties in Beijing during June 1999, J. Geophys. Res., 106 (D16), 17969–17980, 2001.

Cai, H. K., Zhou, R. J., Fu, Y. F., Zheng, Y. Y., and Wang, Y. J.: Cloud-aerosol lidar with or thogonal polarization detection of aerosol optical properties after a crop burning case, Clim. Environ. Res., 16, 469–478, 2011.

Che, H. Z., Zhang, X. Y., Xia, X., Goloub, P., Holben, B., Zhao, H., Wang, Y., Zhang, X. C., Wang, H., Blarel, L., Damiri, B., Zhang, R., Deng, X., Ma, Y., Wang, T., Geng, F., Qi, B., Zhu, J., Yu, J., Chen, Q., and Shi, G.: Ground-based aerosol climatology of China: aerosol optical depths from the China Aerosol Remote Sensing Network (CARSNET) 2002–2013, Atmos. Chem. Phys., 15, 7619–7652, 2015a.

Che, H. Z., Zhao, H. J., Wu, Y. F., Xia, X. A., Zhu, J., Wang, H., Wang, Y. Q., Sun, J. Y., Yu, J., Zhang, X. Y., and Shi, G. Y.: Analyses of aerosol optical properties and direct radiative forcing over urban and industrial regions in Northeast China, Meteorology and Atmospheric Physics, 127(3), 345-354, doi:10.1007/s00703-015-0367-3, 2015c.

Che, H., Wang, Y., and Sun, J.: Aerosol optical properties at Mt. Waliguan observatory, China, Atmos.

662 Environ., 45, 6004–6009, 2011.

663 Che, H., Xia, X., Zhu, J., Li, Z., Dubovik, O., Holben, B., Goloub, P., Chen, H., Estelles, V.,
664 Cuevas-Agulló, E., Blarel, L., Wang, H., Zhao, H., Zhang, X., Wang, Y., Sun, J., Tao, R., Zhang, X.,
665 and Shi, G.: Column aerosol optical properties and aerosol radiative forcing during a serious
666 haze-fog month over North China Plain in 2013 based on ground-based sunphotometer
667 measurements, Atmos. Chem. Phys., 14, 2125–2138, doi:10.5194/acp-14-2125-2014, 2014.

668 Che, H., Xia, X., Zhu, J., Wang, H., Wang, Y., Sun, J., Zhang, X., and Shi, G.: Aerosol optical
669 properties under the condition of heavy haze over an urban site of Beijing, China, Environ. Sci.
670 Pollut. R., 22, 1043–1053, doi:10.1007/s11356-014-3415-5, 2015b.

671 Che, H.,Wang, Y., Sun, J., Zhang, X., Zhang, X., and Guo, J.: Variation of Aerosol Optical Properties
672 over the Taklimakan Desert in China, Aerosol Air Qual. Res., 13, 777–785, 2013.

673 Chiang, C. W., Chen, W. N., Liang, W. A., Das, S. K., and Nee, J. B.: Optical properties of tropospheric
674 aerosols based on measurements of lidar, sun-photometer, and visibility at Chung-Li (25^{o}N, 121^{o}E),
675 Atmos. Environ., 41, 4128-4137, doi:10.1016/j.atmosenv.2007.01.019, 2007.

676 Deng, J. J., Zhang, Y. R., Hong, Y. W., Xu, L. L., Chen, Y. T., Du, W. J., and Chen, J. S.: Optical
677 properties of $PM_{2.5}$ and the impacts of chemical compositions in the coastal city Xiamen in China,
678 Science of the Total Environment, 557-558, 665-675, 2016.

679 Dong, Z. P., Li, X. M., Du, C. L., and, Zhang, G. J.: Study on aerosol optical property in Xi'An Region,
680 Plateau Meteorology, 32(3), 856-864, doi:10.7522/j.issn.1000-0534.2012.00079, 2013.

681 Dubovik, O. and King, M. D.: A flexible inversion algorithm for the retrieval of aerosol optical
682 properties from Sun and sky radiance measurements, J. Geophys. Res., 105, 20673–20696,
683 doi:10.1029/2000JD900282, 2000.

684 Dubovik, O., Sinyuk, A., Lapyonok, T., Holben, B. N., Mishchenko, M., Yang, P., Eck, T. F., Volten, H.,
685 Munoz, O., Veihelmann, B., van der Zande, W. J., Leon, J. F., Sorokin, M., and Slutsker, I.:
686 Application of spheroid models to account for aerosol particle nonsphericity in remote sensing of
687 desert dust, J. Geophys. Res.-Atmos., 111, D11208, doi:10.1029/2005jd006619, 2006.
688 Fan, X. H., Chen, H. B., Xia, X. A., Li, Z. Q., and Cribb, M.: Aerosol optical properties from the
689 Atmospheric Radiation Measurement Mobile Facility at Shouxian. China, J. Geophys. Res., 115,
690 D00K33, doi:10.1029/2010JD014650, 2010.
691 Forster, P., Ramaswamy, V., Artaxo, P., Berntsen, T., Betts, R., Fahey, D. W., Haywood, J., Lean, J.,
692 Lowe, D. C., Myhre, G., Nganga, J., Prinn, R., Raga, G., Schulz, M., and Van Dorland, R.: Changes
693 in atmospheric constituents and in radiative forcing, in: Climate Change 2007: The Physical
694 Science Basis. Contribution of Working Group I to the Fourth Assessment Report of the
695 Intergovernmental Panel on Climate Change, edited by: Solomon, S. et al., Cambridge Univ. Press,
696 Cambridge, UK, 129–234, 2007.
697 Hansen, A. D. A., Rosen, H., and Novakov, T.: The aethalometer: an instrument for the real time
698 measurements of optical absorption by aerosol particles, Sci. Total Environ., 36, 191–196, 1984.
699 He, X., Li, C. C., Lau, A. K. H., Deng, Z. Z., Mao, J. T., Wang, M. H., and Liu, X. Y.: An intensive
700 study of aerosol optical properties in Beijing urban area, Atmos. Chem. Phys., 9, 8903–8915,
701 doi:10.5194/acp-9-8903-2009, 2009.
702 Holben, B. N., Eck, T. F., Slutsker, I., Tanre, D., Buis, J. P., Setzer, A., Vermote, E., Reagan, J. A.,
703 Kaufman, Y. J., Nakajima, T., Lavenu, F., Jankowiak, I., and Smirnov, A.: AERONET-a federated
704 instrument network and data archive for aerosol characterization, Remote Sens. Environ., 66, 1-16,
705 1998.

706 Holler, R., Ito, K., Tohno, S., and Kasahara, M.: Wavelength-dependent aerosol single scattering albedo:
707 measurements and model calculations for a coastal site near the sea of Japan during ACE-Asia, J.
708 Geophys. Res., 108, 8648, doi:10.1029/2002JD003250, 2003.
709 IPCC 2013: Climate Change 2013: The Physical Science Basis. Contribution of Working Group I to the
710 Fifth Assessment Report of the Intergovernmental Panel on Climate Change, edited by: Stocker, T.
711 F., Qin, D., Plattner, G.-K., Tignor, M., Allen, S. K., Boschung, J., Nauels, A., Xia, Y., Bex, V., and
712 Midgley, P. M., Cambridge University Press, Cambridge, UK and New York, NY, USA, 1535 pp.,
713 2013.
714 Jacobson, M. Z.: A physically based treatment of elemental carbon optics: implication for global direct
715 forcing of aerosols, Geophys. Res. Lett., 27, 217-220, 2000.
716 Jacobson, M. Z.: Control of fossil-fuel particulate black carbon and organic matter, possibly the most
717 effective method of slowing global warming, J. Geophys. Res., 107, 4410,
718 doi:10.1029/2001JD001376, 2002.
719 Jiang, Z., Liu, Z., Wang, T., Schwartz, C. S., Lin, H.-C., and Jiang, F.: Probing into the impact of
720 3DVAR assimilation of surface PM_{10} observations over China using process analysis, J. Geophys.
721 Res. Atmos., 118, 6738–6749, doi:10.1002/jgrd.50495, 2013.
722 Khatri, P., Ishizaka, Y., and Takamura, T.: A study on aerosol optical properties in an urban atmosphere
723 of Nagoya, Japan. J. Meteorol. Soc. Jpn., 87 (1), 19-38, 2009.
724 Kiehl, J. T. and Briegleb, B. P.: The relative roles of sulfate aerosols and greenhouse gases in climate
725 forcing, Science, 260, 311–314, 1993.
726 Kuhlmann, J., and Quaas, J.: How can aerosols affect the Asian summer monsoon? Assessment during
727 three consecutive pre-monsoon seasons from CALIPSO satellite data, Atmos. Chem. Phys., 10,

728 4673-4688, doi:10.5194/acp-10-4673-2010, 2010.
729 Li, J., Carlson, B. E., and Lacis, A. A.: Using single-scattering albedo spectral curvature to characterize
730 East Asian aerosol mixtures, J. Geophys. Res. Atmos., 120, 2037–2052, 2015c.
731 Li, J., Wang, W.-C., Liao, H., and Chang, W. Y.: Past and future direct radiative forcing of nitrate
732 aerosol in East Asia, Theor. Appl. Climatol., 121, 445–458, 2015b.
733 Li, S., Wang, T. J., Xie, M., Han, Y., and Zhuang, B. L.: Observed aerosol optical depth and angstrom
734 exponent in urban area of Nanjing, China, Atmos. Environ., 123, 350-356,
735 doi:10.1016/j.atmosenv.2015.02.048, 2015a.
736 Liao, H. and Seinfeld, J. H.: Global impacts of gas-phase chemistry-aerosol interactions on direct
737 radiative forcing by anthropogenic aerosols and ozone, J. Geophys. Res., 110, D18208,
738 doi:10.1029/2005JD005907, 2005.
739 Ma, X. X., Liu, H. N., Liu, J., and Zhuang, B. L.: Sensitivity of climate effects of black carbon in China
740 to its size distributions, Atmospheric Research, 185, 118-130, 2017.
741 Ma, X., and Yu, F.: Effect of spectral dependent surface albedo on Saharan dust direct radiative forcing.
742 Geophys. Res. Lett. 39, L09808, 2012.Madronich, S.: UV radiation in the natural and perturbed
743 atmosphere, In: Tevini,M. (Ed.), UV-B Radiation and Ozone Depletion, Effects on Humans,
744 Animals, Plants, Microorganisms, and Materials, Lewis Publisher, Boca Raton, pp. 17-69, 1993.
745 Markowicz, K. M., Flatau, P. J., Remiszewska, J., Witek, M., Reid, E. A., Reid, J. S., Bucholtz, Z., and
746 Hilben, B.: Observations and modeling of the surface aerosol radiative forcing during UAE. J.
747 Atmos. Sci. 65, 2877-2891, 2008.
748 Menon, S., Hansen, J., Nazarenko, L., and Luo, Y. F.: Climate effects of black carbon aerosols in China
749 and India, Science, 297, 2250–2253, doi:10.1126/science.1075159, 2002.

750 Palancar, G.G., and Toselli, B. M.: Effects of meteorology and tropospheric aerosols on UV-B radiation:
751 a 4-year study. Atmos. Environ. 18, 2749-2757, 2004.
752 Pan, L, Che, H. Z., Geng, F. H., Xia, X. A., Wang, Y. Q., Zhu, C. Z., Chen, M., Gao, W., and Guo, J. P.:
753 Aerosol optical properties based on ground measurements over the Chinese Yangtze Delta Region,
754 Atmos. Environ., 44, 2587-2596, doi:10.1016/j.atmosenv.2010.04.013, 2010.
755 Peng, Z., Liu, Z. Q., Chen, D., and Ban, J. M: Improving PM2:5 forecast over China by the joint
756 adjustment of initial conditions and source emissions with an ensemble Kalman filter, Atmos. Chem.
757 Phys., 17, 4837–4855, 2017.
758 Penner, J. E., Andreae, M., Annegarn, H., Barrie, L., Feichter, J., Hegg, D., Jayaraman, A., Leaitch, R.,
759 Murphy, D., Nganga, J., and Pitari, G.: Aerosols, their direct and indirect effects, in: Climate
760 Change 2001: The Scientific Basis. Contribution of Working Group I to the Third Assessment
761 Report of the Intergovernmental Panel on Climate Change, edited by: Houghton, J. T. et al.,
762 Cambridge University Press, Cambridge, UK and New York, NY, USA, 289–348, 2001.
763 Podgorny, I. A., and Ramanathan, V.: A modeling study of the direct effect of aerosols over the
764 tropical Indian Ocean, J Geophys. Res. 106, D20, 24097–24105, 2001.
765 Qi, B., Hu, D. Y., Che, H. Z., Du, R. G., Wu, Y. F., Xia, X. A., Zha, B., Liu, J., Niu, Y. W., Wang, H.,
766 Zhang, X. Y., and Shi, G. Y.: Seasonal variation of aerosol optical properties in an urban site of the
767 Yangtze Delta Region of China. Aerosol Air Qual. Res., 16, 2884-2896, 2016.
768 Reddy, M. S., Boucher, O., Bellouin, N., Schulz, M., Balkanski, Y., Dufresne, J. L., and Pham, M.:
769 Estimates of global multicomponent aerosol optical depth and direct radiative perturbation in the
770 Laboratoire de Meteorologie Dynamique general circulation model, J. Geophys. Res., 110, D10S16,
771 doi:10.1029/2004JD004757, 2005.

772 Russell, P. B., Kacenelenbogen, M., Livingston, J. M., Hasekamp, O. P., Burton, S. P., Schuster, G. L.,
773 Johnson, M. S., Knobelspiesse, K. D., Redemann, J., Ramachandran, S., and Holben, B.: A
774 multiparameter aerosol classification method and its application to retrievals from spaceborne
775 polarimetry, J. Geophys. Res.-Atmos., 119, 9838–9863, doi:10.1002/2013JD021411, 2014.
776 Sun, H., Pan, Z., and Liu, X.: Numerical simulation of spatial-temporal distribution of dust aerosol and
777 its direct radiative effects on East Asian climate, J. Geophys. Res., 117, D13206,
778 doi:10.1029/2011JD017219, 2012.
779 Tao, R., Che, H. Z., Chen, Q. L., Tao, J., Wang, Y. Q., Sun, J. Y., Wang, H., and Zhang, X. X.: Study of
780 aerosol optical properties based on ground measurements over Sichuan Basin, China, Aerosol and
781 Air Quality Research, 14: 905–915. doi:10.4209/aaqr.2012.07.0200, 2014.
782 Wang, T. J., Zhuang, B. L., Li, S., Liu, J., Xie, M., Yin, C. Q., Zhang, Y., Yuan, C., Zhu, J. L., Ji, L. Q.,
783 and Han, Y.: The interactions between anthropogenic aerosols and the East Asian summer monsoon
784 using RegCCMS, J. Geophys. Res. Atmos., 120, doi:10.1002/2014JD022877, 2015.
785 Wang, Y., Che, H. Z., Ma, J. Z., Wang, Q., Shi, G. Y., Chen, H. B., Goloub, P., and Hao, X. J.: Aerosol
786 radiative forcing under clear, hazy, foggy, and dusty weather conditions over Beijing, China,
787 Geophys. Res. Lett., 36, L06804, doi:10.1029/2009GL037181, 2009.
788 Weingartner, E., Saathoff, H., Schnaiter, M., Streit, N., Bitnar, B., and Baltensperger, U.: Absorption of
789 light by soot particles: determination of the absorption coefficient by means of aethalometers, J.
790 Aerosol Sci., 34, 1445–1463, doi:10.1016/S0021-8502(03)00359-8, 2003.
791 Wu, Y. F., Zhang, R. J., Pu, Y. F., Zhang, L. M., Ho, K. F., and Fu, C. B.: Aerosol optical properties
792 observed at a semi-arid rural site in northeastern China, Aerosol Air Qual. Res., 12, 503–514, 2012.
793 Xia, X. A., Li, Z. Q., Holben, B., Wang, P., Eck, T., Chen, H. B., Cribb, M., and Zhao, Y. X.: Aerosol

794 optical properties and radiative effects in the Yangtze Delta region of China, J. Geophys. Res., 112,
795 D22S12, doi:10.1029/2007JD008859, 2007.
796 Xia, X., Che, H., Zhu, J., Chen, H., Cong, Z., Deng, X., Fan, X., Fu, Y., Goloub, P., Jiang, H., Liu, Q.,
797 Mai, B., Wang, P., Wu, Y., Zhang, J., Zhang, R., and Zhang, X.: Ground-based remote sensing of
798 aerosol climatology in China: aerosol optical properties, direct radiative effect and is
799 parameterization, Atmos. Environ., 214, 243-251, doi:10.1016/j.atmosenv.2015.06.071, 2016.
800 Xu, J., Bergin, M. H., Greenwald, R., Schauer, J. J., Shafer, M. M., Jaffrezo, J. L., and Aymoz, G.:
801 Aerosol chemical, physical, and radiative characteristics near a desert source region of Northwest
802 China during ACE-Asia, J. Geophys. Res., 109, D19S03, doi:10.1029/2003JD004239, 2004.
803 Xu, J., Bergin, M. H., Yu, X., Liu, G., Zhao, J., Carrico, C. M., and Baumann, K.: Measurement of
804 aerosol chemical, physical and radiative properties in the Yangtze delta region of China, Atmos.
805 Environ., 36, 161–173, 2002.
806 Xu, J., Tao, J., Zhang, R., Cheng, T., Leng, C., Chen, J., Huang, G., Li, X., and Zhu, Z.: Measurements
807 of surface aerosol optical properties in winter of Shanghai, Atmos. Res., 109-110, 25–35, 2012.
808 Xu, X.: Retrieval of aerosol microphysical properties from AERONET photolarimetric measurements.
809 PhD diss., Department of Earth and Atmospheric Sciences, University of Nebraska-Lincoln, 2015.
810 Yan, P., Tang, J., Huang, J., Mao, J. T., Zhou, X.J., Liu, Q., Wang, Z. F., and Zhou, H. G.: The
811 measurement of aerosol optical properties at a rural site in Northern China, Atmos. Chem. Phys., 8,
812 2229–2242, doi:10.5194/acp-8-2229-2008, 2008.
813 Yu, J., Che, H. Z., Chen, Q. L., Xia, X. A., Zhao, H. J., Wang, H., Wang, Y. Q., Zhang, X. X., and Shi,
814 G. Y.: Investigation of aerosol optical depth (AOD) and Ångström exponent over the desert region
815 of northwestern China based on measurements from the China Aerosol Remote Sensing Network

(CARSNET), Aerosol Air Qual. Res., 15, 2024-2036, doi:10.4209/aaqr.2014.12.0326, 2015.

Yu, X. N., Ma, J., Kumar, K. R., Zhu, B., An, J. L., He, J. Q., and Li, M.: Measurement and analysis of surface aerosol optical properties over urban Nanjing in the Chinese Yangtze River Delta, Sci. Total Environ., 542, 277-291, 2016.

Yu, X. N., Zhu, B., Yin, Y., Fan, S. X., and Chen, A. J.: Seasonal variation of columnar aerosol optical properties in Yangtze River Delta in China, Adv. Atmos. Sci., 28(6), 1326-1335, doi:10.1007/s00376-011-0158-9, 2011.

Zhang, L., Sun, J. Y., Shen, X. J., Zhang, Y. M., Che, H., Ma, L. Q., Zhang, Y. W., Zhang, X. Y., and Ogren, J. A.: Observations of relative humidity effects on aerosol light scattering in the Yangtze River Delta of China, Atmos. Chem. Phys., 15, 8439–8454, 2015.

Zhang, Q., Streets, D. G., Carmichael, G. R., He, K. B., Huo, H., Kannari, A., Klimont, Z., Park, I. S., Reddy, S., Fu, J. S., Chen, D., Duan, L., Lei, Y., Wang, L. T., and Yao, Z. L.: Asian emissions in 2006 for the NASA INTEX-B mission, Atmos. Chem. Phys., 9, 5131–5153, doi:10.5194/acp-9-5131-2009, 2009.

Zhang, W., Hu, B., Chen, C. H., Du, P., Zhang, L., and Feng, G. H.: Scattering properties of atmospheric aerosols over Lanzhou City and applications using an integrating nephelometer, Adv. Atmos. Sci., 21(6), 848–856, 2004.

Zhang, X. Y., Wang, Y. Q., Niu, T., Zhang, X. C., Gong, S. L., Zhang, Y. M., and Sun, J. Y.: Atmospheric aerosol compositions in China: Spatial/temporal variability, chemical signature, regional haze distribution and comparisons with global aerosols, Atmos. Chem. Phys., 12, 779–799, doi:10.5194/acp-12-779-2012, 2012.

Zhao, H. J., Che, H. Z., Zhang, X. Y., Ma, Y. J., Wang, Y. F., Wang, X. X., Liu, C., Hou, B., and Che,

X. C.: Aerosol optical properties over urban and industrial region of Northeast China by using ground-based sun-photometer Measurement, Atmos. Environ., 75, 270-278. doi:10.1016/j.atmosenv.2013.04.048, 2013.

Zheng, Y., Che, H. Z., Zhao, T. L., Xia, X. A., Gui, K., An, L. C., Qi, B., Wang, H., Wang, Y. Q., Yu, J., and Zhang, X. Y.: Aerosol optical properties during the World Athletics Championships and Victory Day Military Parade over Beijing in August and September 2015, Atmosphere, 7(3), 47; doi:10.3390/ atmos7030047, 2016.

Zhu, J., Che, H. Z., Xia, X. A., Chen, H. B., Goloub, P., and Zhang, W. X.: Column-integrated aerosol optical and physical properties at a regional background atmosphere in North China Plain, Atmos. Environ., 84, 54-64, doi:10.1016/j.atmosenv.2013.11.019, 2014.

Zhu, J., Wang, T., Talbot, R., Mao, H., Hall, C. B., Yang, X., Fu, C., Zhuang, B., Li, S., Han, Y., and Huang, X.: Characteristics of atmospheric Total Gaseous Mercury (TGM) observed in urban Nanjing, China, Atmos. Chem. Phys., 12, 12103–12118, doi:10.5194/acp-12-12103-2012, 2012.

Zhuang, B. L., Li, S., Wang, T. J., Deng, J. J., Xie, M., Yin, C. Q., and Zhu, J. L.: Direct radiative forcing and climate effects of anthropogenic aerosols with different mixing states over China, Atmos. Environ., 79, 349–361, doi:10.1016/j.atmosenv.2013.07.004, 2013a.

Zhuang, B. L., Liu, Q., Wang, T. J., Yin, C. Q., Li, S., Xie, M., Jiang, F., and Mao, H. T.: Investigation on semi-direct and indirect climate effects of fossil fuel black carbon aerosol over China, Theor. Appl. Climatol., 114, 651–672, doi:10.1007/s00704-013-0862-8, 2013b.

Zhuang, B. L., Wang, T. J., Li, S., Liu, J., Talbot, R., Mao, H. T., Yang, X. Q., Fu, C. B., Yin, C. Q., Zhu, J. L., Che, H. Z., and Zhang, X. Y.: Optical properties and radiative forcing of urban aerosols in Nanjing, China, Atmos. Environ., 83, 43–52, 2014a.

Zhuang, B. L., Wang, T. J., Liu, J., Li, S., Xie, M., Han, Y., Chen, P. L., Hu, Q. D., Yang, X. Q., Fu, C. B., Zhu, J. L.: The surface aerosol optical properties in urban area of Nanjing, west Yangtze River Delta, China, Atmos. Chem. Phys., 17, 1143–1160, 2017.

Zhuang, B. L., Wang, T. J., Liu, J., Li, S., Xie, M., Yang, X. Q., Fu, C. B., Sun, J. N., Yin, C. Q., Liao, J. B., Zhu, J. L., and Zhang, Y.: Continuous measurement of black carbon aerosol in urban Nanjing of Yangtze River Delta, China, Atmos. Environ., 89, 415–424, 2014b.

Zhuang, B. L., Wang, T. J., Liu, J., Ma, Y., Yin, C. Q., Li, S., Xie, M., Han, Y., Zhu, J. L., Yang, X. Q., and Fu, C. B.: Absorption coefficient of urban aerosol in Nanjing, west Yangtze River Delta, China, Atmos. Chem. Phys., 15, 13633–13646, 2015.

Figure captions:

Figure 1. Monthly variations of the total (a), scattering (b), and absorbing (c) aerosol optical depths (AOD) at 550 nm, including the ratio of the AOD in fine or coarse mode to the AOD in all mode (line with triangle markers in green) in urban area of Nanjing. The 10th, 25th, median, 75th, 90th percentile values of the all mode AOD are presented as box plots. The monthly means of the all mode AODs are presented as cycle markers in gray.

Figure 2. Monthly variations of the total (a), scattering (b), and absorbing aerosol (c) Ångström exponents (AE) at 440/870 nm for the all, fine and coarse modes in urban area of Nanjing.

Figure 3. Monthly variations of the all, fine, and coarse mode aerosol single scattering albedo (SSA) at 550 nm (a) and the aerosol refractive indices at 440 nm (b) in urban area of Nanjing.

Figure 4. Frequency distributions of the size dependent AODs at 550 nm (a), AEs at 440/870 nm (b), SSAs at 550 nm (c) as well as the real and imaginary parts at 440 nm (c) in urban area of Nanjing.

882 Figure 5. Comparisons between CE-318 and MODIS based AOD at 550 nm and between AE at
883 440/870 nm for CE-318 and at 412/470 nm for MODIS in Nanjing.

884 Figure 6. Comparisons between the absorbing aerosol optical depth (AAOD) at 550 nm from CE-318
885 and surface absorption coefficient (AAC) at 520 nm from AE-31 (a) and between the column AAE at
886 440/870 nm from CE-318 and surface AAE at 470/880 nm from AE-31 (b) in urban Nanjing.

887 Figure 7. The averaged aerosol volume size ($\mu m^3/\mu m^2$) distributions in different seasons (a) and in
888 different AOD levels in urban Nanjing.

889 Figure 8. Seasonal variations of the effective (a, μm) and mean (b, μm) radius of aerosols as well as the
890 aerosol volume concentrations (c, $\mu m^3/cm^3$) in the all, fine and coarse modes in urban Nanjing.

891 Figure 9. Relationships between the monthly mean values of 491 nm SSA and total Ångström exponent
892 (AE) at 491/870 nm (a), between the monthly mean values of the real refractive index at 670 nm and
893 AE at 491/870 nm (b), and between the monthly mean values of the SSA difference (870–491 nm) and
894 AE at 491/870 nm (c).

895 Figure 10. Distribution of the SSA and AAOD Curvatures in urban area of Nanjing under different
896 spectral SSA conditions, including monotonically decreasing, increasing SSA spectra and peaked SSA
897 spectra.

898 Figure 11. The aerosol vertical proportions (%) from CALIPSO, Polarization-Raman Lidar and their
899 average in Nanjing.

900 Figure 12. Seasonal variations of the clear sky aerosol direct radiative forcing (DRF, W/m^2) at both
901 TOA (a~c) and the surface (d~f). The DRFs of the total (a, d), scattering (b, e) and absorbing (c, f)
902 aerosols in the all, fine and coarse modes are all investigated in urban Nanjing.

903 Figure 13. Comparisons in the absorbing aerosol DRFs (W/m^2) between from BC SSA and from the

total aerosol DRF minus the scattering one.

Figure 14. Sensitivities of the TOA and the surface aerosol DRFs (day time, W/m^2) to the different aerosol profiles in clear conditions, for the total, scattering and absorbing aerosols.

Tables:

Table 1 Statistical summary of the columnar aerosol optical properties in urban area of Nanjing

Factors	Max	Min	Mean±SD	Meadian
550 nm AOD	2.3208	0.2723	0.6494±0.2852	0.5912
550 nm FAOD	2.2216	0.1468	0.5257±0.2806	0.4479
550 nm CAOD	0.9891	0.0139	0.1237±0.1076	0.0858
550 nm SAOD	2.2744	0.2443	0.6059±0.2747	0.5492
550 nm FSAOD	2.1459	0.1435	0.5014±0.2713	0.4263
550 nm CSAOD	0.8842	0.0113	0.1045±0.0957	0.0705
550 nm AAOD	0.2304	0.0020	0.0435±0.0240	0.0421
550 nm FAAOD	0.1424	0.0005	0.0244±0.0175	0.0208
550 nm CAAOD	0.1163	0.0009	0.0192±0.0145	0.0156
440/870 nm AE	1.9100	0.3085	1.2045±0.2856	1.2436
440/870 nm FAE	2.3625	0.3565	1.7083±0.2979	1.7364
440/870 nm CAE	-0.0789	-0.3805	-0.1876±0.0430	-0.1898
440/870 nm SAE	1.9916	0.2958	1.1976±0.3085	1.2386
440/870 nm FSAE	2.3653	0.3463	1.7102±0.2980	1.7368
440/870 nm CSAE	-0.1048	-0.7111	-0.3838±0.1017	-0.3864
440/870 nm AAE	3.4619	0.1483	1.3237±0.4820	1.2587
440/870 nm FAAE	4.5118	0.2912	1.7521±0.6470	1.6516
440/870 nm CAAE	3.1264	-0.0844	0.8748±0.4589	0.8209
550 nm SSA	0.9959	0.8053	0.9297±0.0335	0.9305
550 nm FSSA	0.9974	0.8388	0.9524±0.0261	0.9549
550 nm CSSA	0.9835	0.5898	0.8208±0.0754	0.8225
440 nm Real part	1.6000	1.3300	1.4423±0.0638	1.4374
440 nm Imaginary part	0.0301	0.0005	0.0084±0.0047	0.0078

AOD: Aerosol optical depth
FAOD: Fine aerosol optical depth
CAOD: Coarse aerosol optical depth
SAOD: Scattering aerosol optical depth
FSAOD: Scattering aerosol optical depth in fine mode
CSAOD: Scattering aerosol optical depth in coarse mode
AAOD: Absorbing aerosol optical depth
FAAOD: Absorbing aerosol optical depth in fine mode
CAAOD: Absorbing aerosol optical depth in coarse mode
AE: Ångström exponent of total aerosols
FAE: Ångström exponent of fine aerosols
CAE: Ångström exponent of coarse aerosols
SAE: Ångström exponent of scattering aerosols
FSAE: Ångström exponent of scattering aerosols in fine mode
CSAE: Ångström exponent of scattering aerosols in coarse mode

AAE: Ångström exponent of absorbing aerosols
FAAE: Ångström exponent of absorbing aerosols in fine mode
CAAE: Ångström exponent of absorbing aerosols in coarse mode
SSA: Single scattering albedo of total aerosols
FSSA: Single scattering albedo of fine aerosols
CSSA: Single scattering albedo of coarse aerosols

Table 2 Seasonal mean±SD of the columnar aerosol optical properties in urban area of Nanjing

Factors	MAM	JJA	SON	DJF
550 nm AOD	0.6788±0.2919	0.7508±0.3749	0.5866±0.2447	0.6560±0.2976
550 nm FAOD	0.4739±0.2613	0.6798±0.3793	0.5149±0.2462	0.5687±0.2978
550 nm CAOD	0.2048±0.1356	0.0710±0.0599	0.0717±0.0346	0.0873±0.0685
550 nm SAOD	0.6284±0.2835	0.7031±0.3728	0.5495±0.2342	0.6157±0.2829
550 nm FSAOD	0.4529±0.2552	0.6463±0.3760	0.4901±0.2366	0.5428±0.2846
550 nm CSAOD	0.1756±0.1225	0.0568±0.0497	0.0593±0.0315	0.0728±0.0601
550 nm AAOD	0.0503±0.0208	0.0477±0.0307	0.0372±0.0200	0.0403±0.0271
550 nm FAAOD	0.0211±0.0125	0.0335±0.0212	0.0248±0.0157	0.0259±0.0211
550 nm CAAOD	0.0292±0.0165	0.0142±0.0137	0.0124±0.0066	0.0144±0.0111
440/870 nm AE	0.9915±0.2385	1.2174±0.2639	1.3744±0.1907	1.3134±0.2461
440/870 nm FAE	1.7474±0.2896	1.4701±0.3075	1.7408±0.2582	1.6935±0.3019
440/870 nm CAE	-0.1998±0.0352	-0.1699±0.0471	-0.1862±0.0424	-0.1807±0.0464
440/870 nm SAE	0.9812±0.2687	1.2733±0.2950	1.3824±0.2043	1.2956±0.2697
440/870 nm SFAE	1.7555±0.2862	1.5218±0.3397	1.7492±0.2545	1.6809±0.3039
440/870 nm SCAE	-0.3752±0.0743	-0.2815±0.0678	-0.3797±0.0991	-0.4016±0.1162
440/870 nm AAE	1.1885±0.4500	0.7971±0.2657	1.3290±0.4533	1.5007±0.4520
440/870 nm FAAE	1.7352±0.6059	0.9943±0.2672	1.6715±0.5970	1.8947±0.6545
440/870 nm CAAE	0.8542±0.4665	0.3771±0.2753	0.8312±0.4479	0.9798±0.4235
550 nm SSA	0.9204±0.0313	0.9241±0.0422	0.9348±0.0331	0.9378±0.0331
550 nm FSSA	0.9527±0.0237	0.9405±0.0356	0.9518±0.0253	0.9555±0.0265
550 nm CSSA	0.8340±0.0628	0.7868±0.0953	0.8115±0.0752	0.8211±0.0810
440 nm Real part	1.4647±0.0628	1.4075±0.0609	1.4252±0.0602	1.4404±0.0582
440 nm Imaginary part	0.0084±0.0040	0.0083±0.0052	0.0080±0.0044	0.0083±0.0053

Table 3. The annual mean aerosol direct radiative forcing (W/m^2) in urban area of Nanjing

Species	Clear sky	
	TOA	Surface
TA	-10.69±3.37	-25.54±2.83
FA	-11.17±3.09	-21.37±2.78
CA	-0.33±0.60	-6.15±2.90
SA	-16.45±2.81	-17.17±2.96
FSA	-15.08±3.18	-15.74±3.35
CSA	-2.31±1.18	-2.42±1.24
AA	5. 76±1.27	-8.38±1.56
FAA	3.91±0.95	-5.63±1.16
CAA	1.99±1.07	-3.73±1.71

TA: Total aerosols

FA: Fine aerosols

CA: Coarse aerosols

SA: All scattering aerosols

FSA: Scattering aerosols in fine mode

CSA: Scattering aerosols in coarse mode

AA: All absorbing aerosols' forcing

FAA: Fine absorbing aerosols' forcing

CAA: Coarse absorbing aerosols' forcing

Figures:

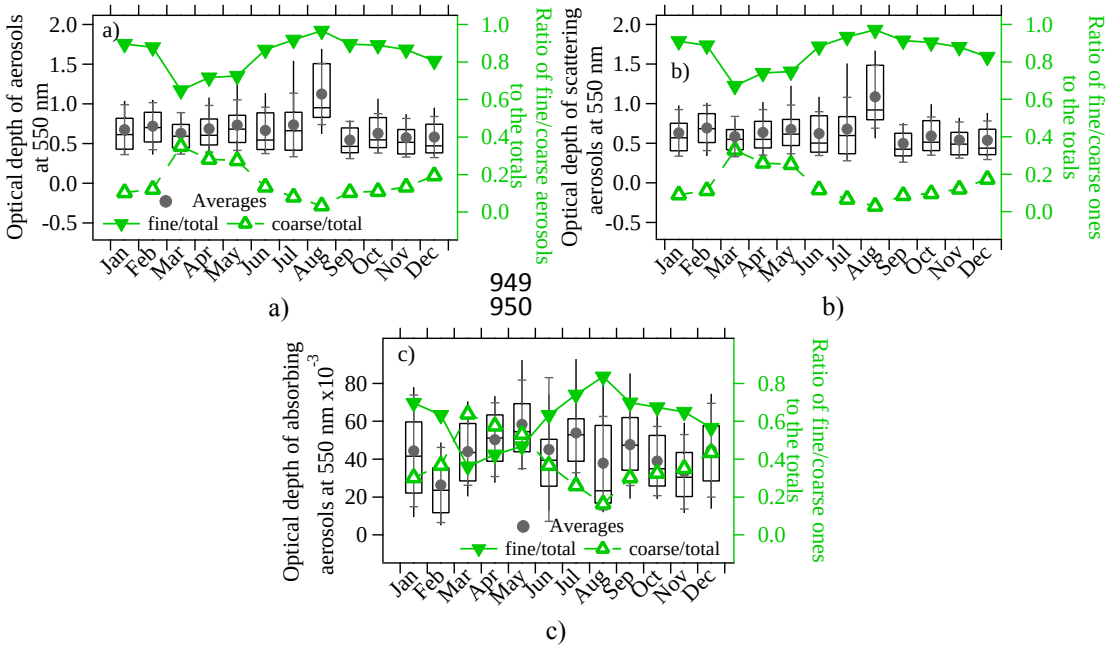

a) b) c)

Figure 1.

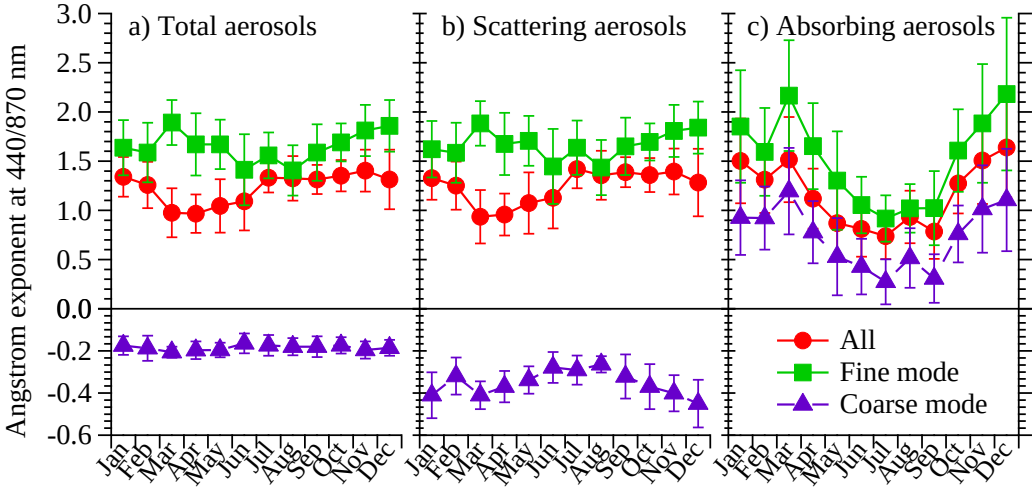

Figure 2.

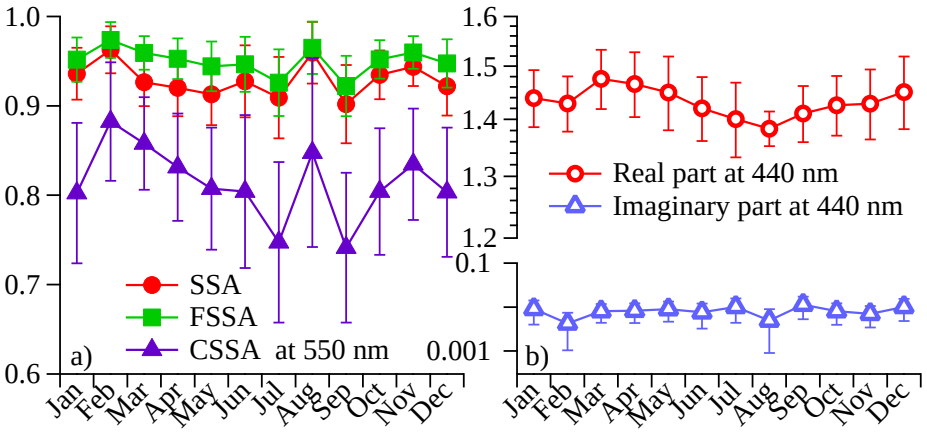

Figure 3

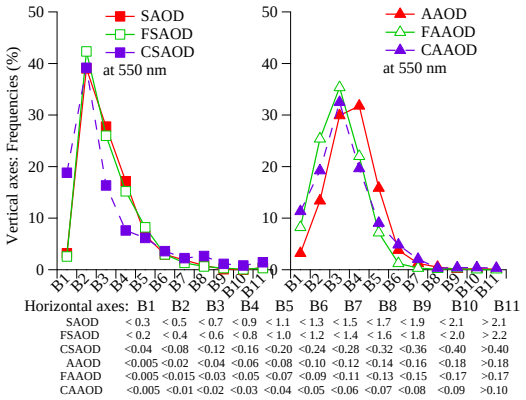

a)

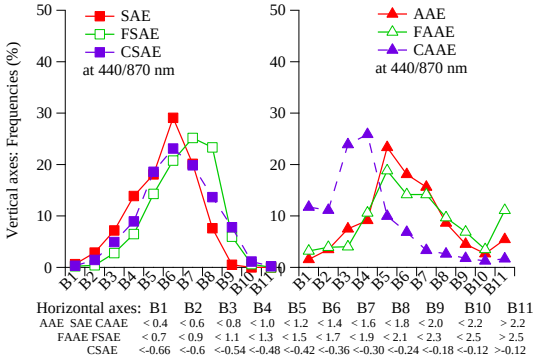

b)

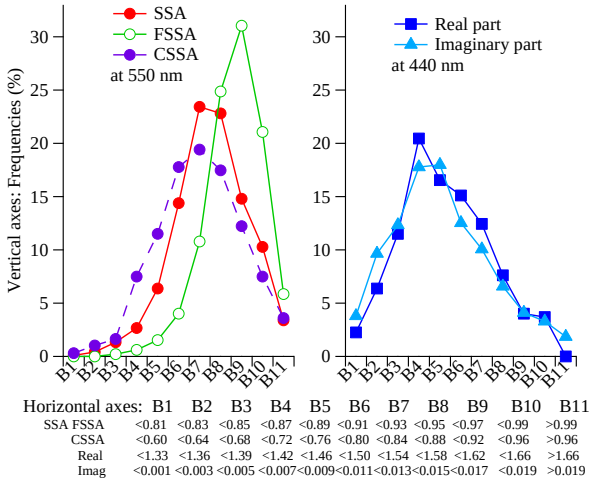

c)

Figure 4

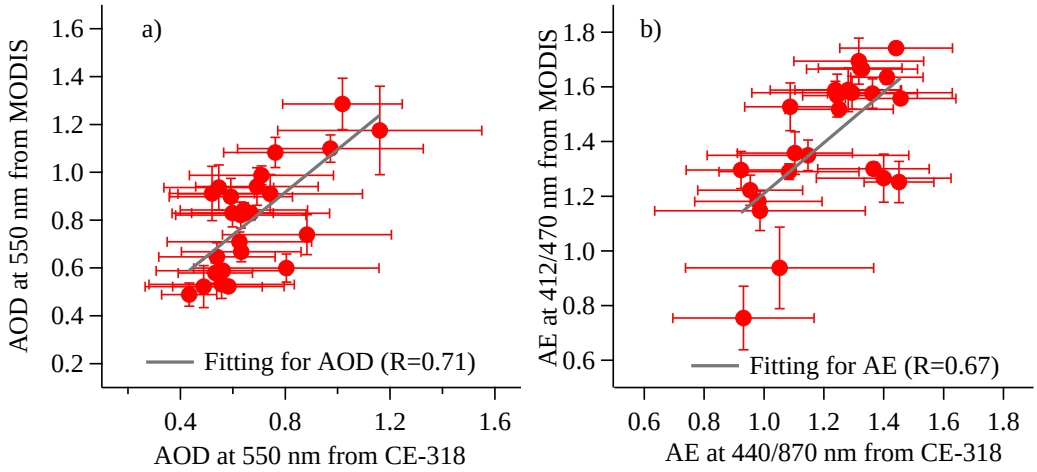

970

971 Figure 5

972

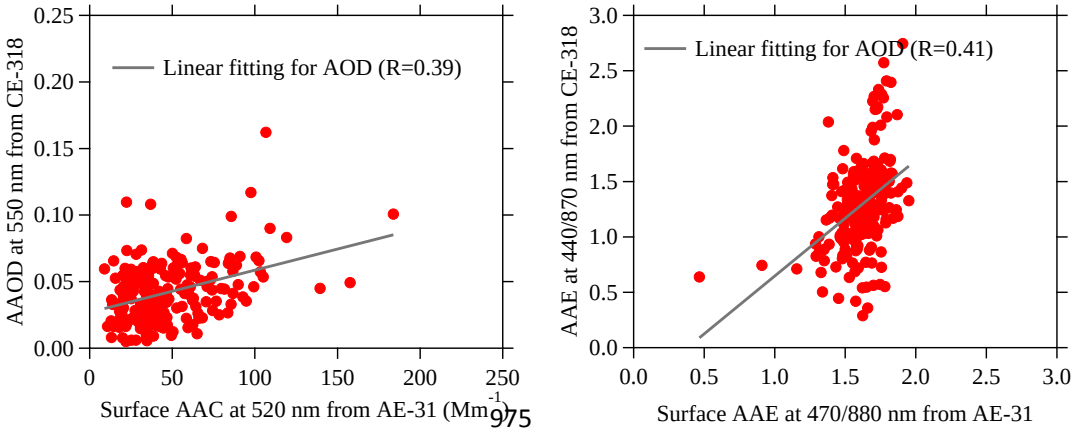

973 974 a) 975 976 b)

977 Figure 6

978

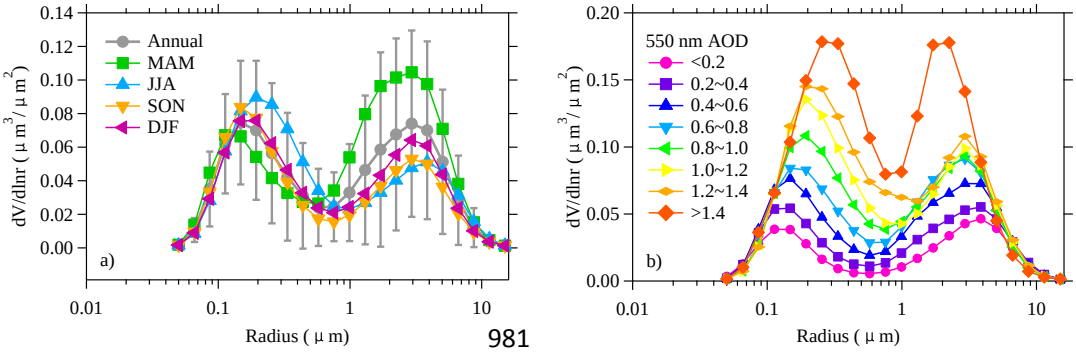

979 980 a) 981 982 b)

983 Figure 7

984

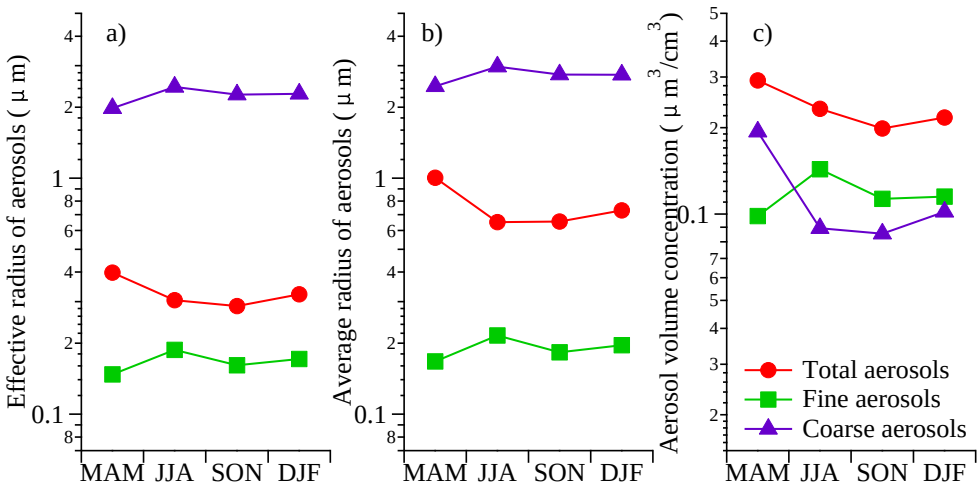

985

986 Figure 8

987

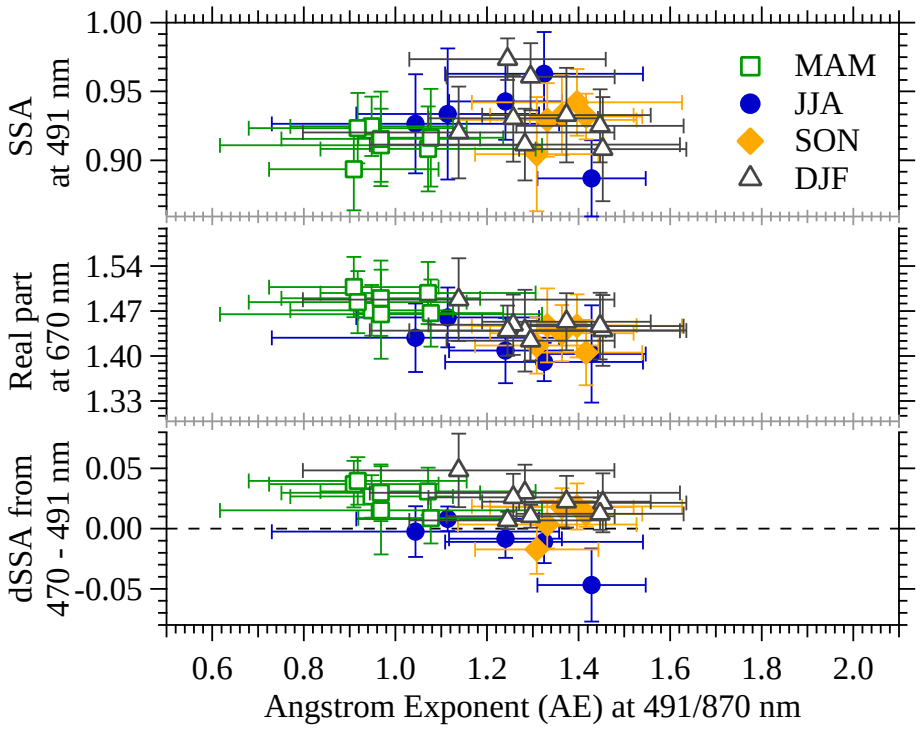

988

989 Figure 9

990

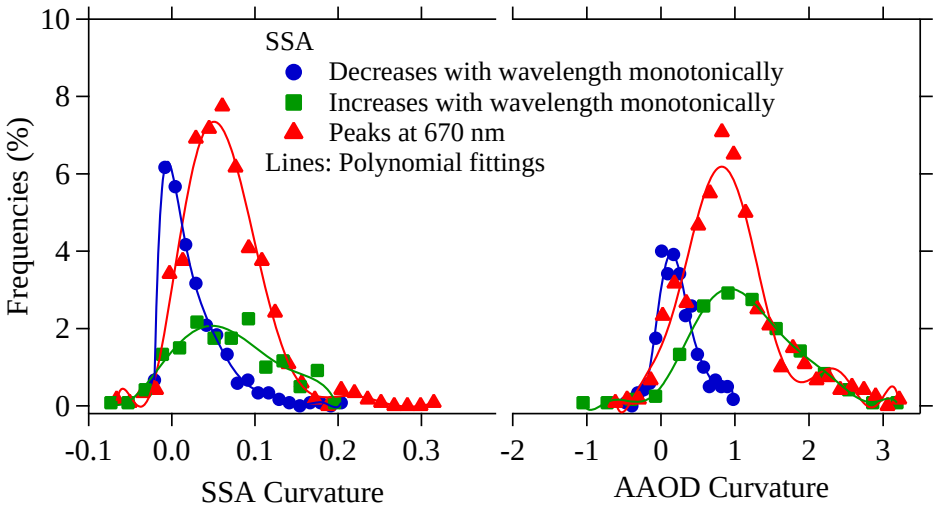

Figure 10

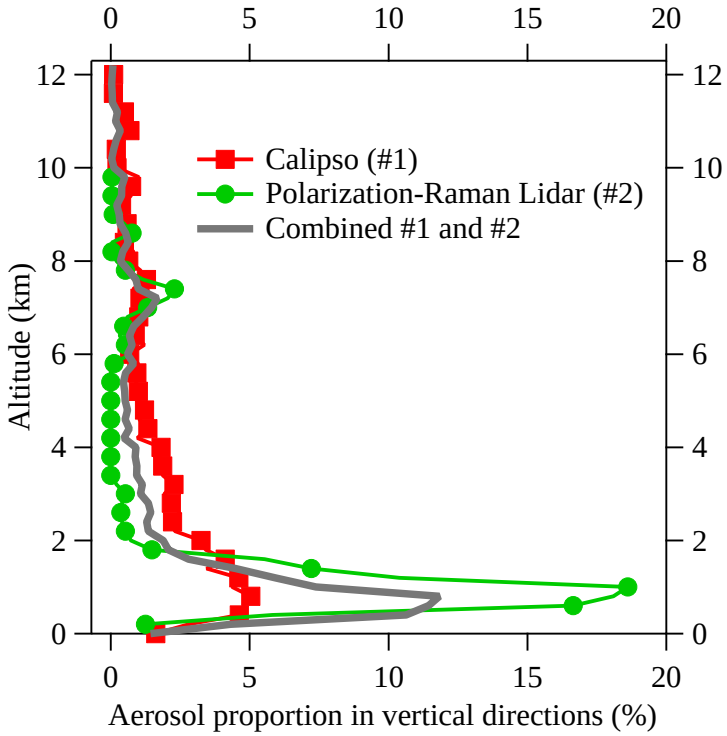

Figure 11

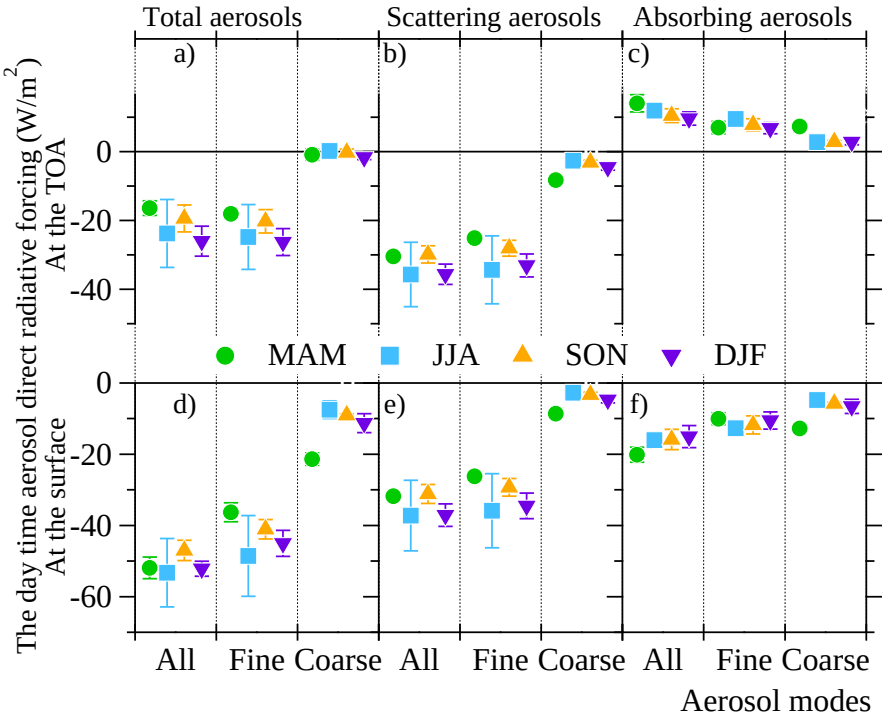

997

998 Figure 12

999

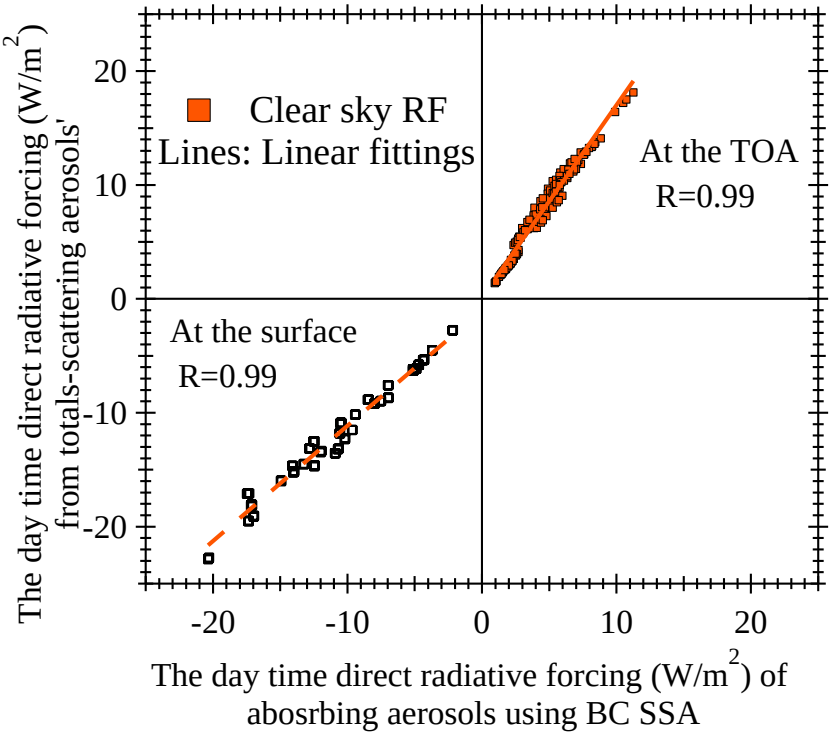

1000

1001 Figure 13

1002

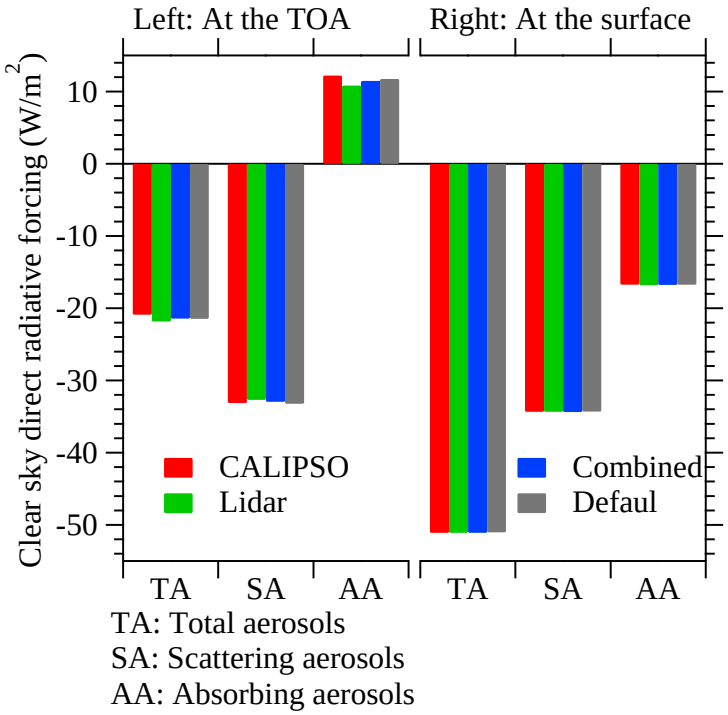

1003

1004 Figure 14

1005

1006